



HAL
open science

Impact of gneissic layering and localized incipient melting upon melt flow during experimental deformation of migmatites

Anne-Céline Ganzhorn, Pierre Trap, Laurent Arbaret, Rémi Champallier, Julien Fauconnier, Loic Labrousse, Gaëlle Prouteau

► To cite this version:

Anne-Céline Ganzhorn, Pierre Trap, Laurent Arbaret, Rémi Champallier, Julien Fauconnier, et al.. Impact of gneissic layering and localized incipient melting upon melt flow during experimental deformation of migmatites. *Journal of Structural Geology*, 2016, 85, pp.68-84. 10.1016/j.jsg.2016.02.004 . insu-01275193

HAL Id: insu-01275193

<https://insu.hal.science/insu-01275193>

Submitted on 17 Feb 2016

HAL is a multi-disciplinary open access archive for the deposit and dissemination of scientific research documents, whether they are published or not. The documents may come from teaching and research institutions in France or abroad, or from public or private research centers.

L'archive ouverte pluridisciplinaire **HAL**, est destinée au dépôt et à la diffusion de documents scientifiques de niveau recherche, publiés ou non, émanant des établissements d'enseignement et de recherche français ou étrangers, des laboratoires publics ou privés.



Distributed under a Creative Commons Attribution - NonCommercial - NoDerivatives 4.0 International License

Highlights :

- Purpose: examine experimental control of anisotropies on melt flow in migmatites.
- Experiments on a homogeneous gneiss and one with strong mineral layering.
- Initial anisotropy strongly controls melt flow and segregation at sample-scale.
- Initial anisotropy also controls deformation distribution and its partitioning.
- Boudinage occurs in the gneiss with mineral layering.

1 Title: Impact of gneissic layering and localized incipient melting upon melt flow during
2 experimental deformation of migmatites

3

4 Ganzhorn A.C.*_{a,b,c,d}, Trap P._e, Arbaret L._{b,c,d}, Champallier R._{b,c,d}, Fauconnier J._a, Labrousse
5 L._a and Prouteau G._{b,c,d}.

6

7 _a Sorbonne Universités, UPMC Univ Paris 06, CNRS, Institut des Sciences de la Terre de
8 Paris (iSTeP), 4 place Jussieu 75005 Paris, France

9 _b Univ. d'Orléans, UMR 7327, ISTO, F-45071 ORLEANS.

10 _c CNRS/INSU, UMR 7327, ISTO, F-45071 ORLEANS.

11 _d BRGM, ISTO, UMR 7327, F-45071 ORLEANS.

12 _e Université de Franche Comté, UMR 6249, Laboratoire Chrono-environnement, F-25030
13 BESANCON.

14

15 * anneceline.ganzhorn@gmail.com +33 (0)1 44 27 49 04

16 pierre.trap@univ-fcomte.fr

17 Laurent.arbaret@univ-orleans.fr

18 remi.champallier@cnrs-orleans.fr

19 julien.fauconnier@upmc.fr

20 loic.labrousse@upmc.fr

21 gaelle.prouteau@cnrs-orleans.fr

22

23 Keywords: anisotropy, natural gneiss, pure-shear deformation, partially molten

24 Abstract:

25 In this study, we test experimentally the role of compositional layering as a key parameter for
26 controlling melt flow in a natural migmatite during coaxial deformation. We performed in –
27 situ pure-shear experiments on two natural gneisses. The first gneiss is weakly foliated with
28 minerals homogeneously distributed. The second gneiss shows a pronounced compositional
29 layering of alternating quartz – feldspar – rich and biotite – muscovite – rich layers.
30 Experimental conditions were selected to obtain homogeneous melt distribution in the
31 homogeneous gneiss and heterogeneous melt distribution in the layered gneiss. Initial melt
32 distribution is not modified by deformation in experiments on the homogeneous gneiss,
33 implying that melting products did not migrate from their initiation sites. In contrast, melt
34 flowed in shear zones or in inter-boudin positions during experimental deformation of the
35 heterogeneous gneiss. These experiments attest to the strong influence of initial gneissic
36 layering on melting pattern, melt segregation and flow during deformation of partially molten
37 rocks.

38

39 ***1. Introduction***

40 Within the crust, partial melting is the main geological process responsible for
41 production of leucogranites, crustal differentiation (Rudnick, 1995) and major changes in
42 crustal strength (Rosenberg & Handy, 2005). Field evidence shows that exhumation of high-
43 pressure metamorphic rocks or extrusion of large tectonic slices are facilitated when the crust
44 reaches its solidus (e.g. Labrousse *et al.*, 2011; Trap *et al.*, 2011). Magneto-telluric (Hashim
45 *et al.*, 2013) and seismic (Nelson *et al.*, 1996) surveys in the North-West Himalaya seem to
46 confirm the presence of a partially molten crust at depth, which are responsible for large-scale
47 lateral flow of the Eurasian crust (Caldwell *et al.*, 2009). At smaller scale, many field
48 observations within migmatitic terrains emphasize the feedback relationship between crustal

49 weakening and the production, segregation and flow of silicate melt (e.g. Brown & Solar,
50 1998).

51 Melt fraction is documented as the first parameter controlling mechanical behaviour
52 and localization of deformation of partially molten aggregates in experimental studies (e.g.
53 Misra *et al.*, 2009). Melt fraction is inferred to have a drastic weakening effect on bulk rock
54 strength (Arzi, 1978; Van der Molen & Paterson, 1979; Rutter *et al.*, 2006). Rosenberg &
55 Handy (2005) showed that 10% partial melting of a dry aplite leads to a strength drop from
56 820 MPa down to 80 MPa in experimental conditions. This first order of magnitude in
57 strength drop is expected to represent a two orders of magnitude drop in effective viscosity
58 for bulk non-Newtonian behaviour with stress exponent $n=3$.

59 Melt viscosity also influences the rheological behaviour of partially molten rocks. It
60 depends mostly on melt silica and water contents, as well as temperature. The addition of 1
61 wt% H₂O to a dry haplogranite at 800°C can induce a viscosity drop from 10¹³ Pa.s to 10⁷
62 Pa.s (Dingwell *et al.*, 1996). Similarly, hydrated melts (1 wt % H₂O and above) maintain
63 substantially equivalent low viscosities (between 10⁶ and 10⁷ Pa.s). In contrast, at similar
64 conditions, an increase of 100°C in melt temperature, which represents the actual variation
65 tested in our experiments, induces less than a one-order viscosity drop for hydrated
66 haplogranite melts (Dingwell *et al.*, 1996).

67 Melt distribution is also a major parameter that controls rock strength, responsible for
68 local changes on melt percentage. In particular, a strength drop occurs for a 10% melt fraction
69 when full connectivity of melt pockets is achieved in experiments (Rosenberg & Handy,
70 2005). Grain-scale surface energy (Cooper & Kohlstedt, 1984; Laporte & Watson, 1995),
71 differential stress (Daines & Kohlstedt, 1997; Zimmerman *et al.*, 1999) and finite deformation
72 magnitude (Kohlstedt & Zimmerman, 1996) have been recognized as controlling parameters
73 for melt distribution. In addition, Tumarkina *et al.* (2011) argued that protolith anisotropy, in

74 particular foliation orientation, is critical for partial melting rate. Yet, anisotropy seems to
75 have little impact on rheological behaviour of partially molten rocks although it may
76 influence their behaviour in sub-solidus domains (Holyoke & Rushmer, 2002). According to
77 Marchildon & Brown (2003) the distribution of leucosomes within migmatites is controlled
78 by protolith anisotropy rather than by regional stresses. With prograde metamorphism,
79 incipient partial melting leads to the formation of metatexites where paleosome dominates.
80 Metatexites are typically heterogeneous with leucosomes (crystallized melt) arranged in a
81 planar manner and oriented parallel to the protolith planar anisotropy, i.e.
82 compositional/gneissic layering (Marchildon & Brown, 2003; Sawyer, 2008). Thus, inherited
83 protolith planar fabric and related melt distribution after incipient melting may be an
84 important parameter to consider when studying strength of partially molten continental crust
85 and related melt flow.

86 In this contribution, we test the impact of incipient melt distribution as a function of
87 host rock texture (isotropic vs anisotropic) for the deformation of partially molten rocks
88 (migmatites) and melt flow. Two sets of pure-shear experiments were performed on two
89 natural gneisses using a Paterson apparatus. We focus on natural gneisses to avoid artificial
90 porosity, potentially high in synthetic material (up to 15%; Misra *et al.*, 2014) that may
91 disturb melt distribution. One natural gneiss shows a pronounced gneissic layering whereas
92 the other is compositionally homogeneous, so that we could document changes in melt
93 distribution as a function of the fabric of the starting gneiss for an experiment. In addition,
94 incipient melt distribution, homogenous *vs* heterogeneous, was controlled using different
95 experimental conditions, i.e. temperature and hydration, to promote water – present and
96 muscovite – dehydration melting reactions and prevent other melting reactions, in particular,
97 biotite – dehydration melting. Homogeneous gneiss was deformed at relatively low
98 temperature (850°C and below), in hydrated and dry conditions, while heterogeneous gneiss

99 was experimented at higher temperature (850°C and above) and dry conditions. One
100 experiment set-up (850°C, dry conditions) is common to both experiment series. The
101 comparison of deformation patterns and melt distributions observed in our experiments allow
102 to discuss the impact of the inherited gneissic layering and related melt distribution on melt
103 flow and deformation of partially molten rocks.

104

105 ***2. Starting materials***

106 Starting materials are two natural gneisses, one homogeneous, weakly foliated gneiss
107 (NOP1) with no compositional layering and one heterogeneous gneiss (PX28) with a strong
108 gneissic layering (Fig. 1). For both starting materials, we also choose experimental conditions
109 to restrain melt production to water – present and to muscovite – dehydration melting
110 reactions, and prevent biotite – dehydration melting. This approach required to adjust
111 experimental conditions using different temperatures with addition of free water for some
112 experiments. The experimental set up were designed to work with two texturally different
113 migmatites, one with a homogenous distribution of melt (in NOP1) and one with a layered-
114 type distribution of melt (in PX28).

115

116 *2.1 Homogeneous gneiss: sample NOP1*

117 The homogeneous gneiss (NOP1) is a quartzo-feldspathic two – mica gneiss, sampled
118 in the inland of the Western Gneiss Region in Norway (N62°05'29'' E006°51'976'',
119 UTM32). Modal composition is 45% quartz, 20% muscovite, 20% biotite, and 15%
120 plagioclase. Accessory minerals are Fe-Ti oxides and zircons. Minerals are homogeneously
121 distributed at sample scale with a weak foliation marked by preferred orientation of micas and
122 elongated quartz grains and aggregates (Fig. 1a). The typical rock fabric is made of 1 mm
123 thick and up to 5 mm long quartz aggregates (composed of grains with maximum length

124 about 500 μm to 1 mm) surrounded by grains of micas and plagioclase of ca. 100 μm in size
125 and even locally smaller (Fig. 1b).

126 *'Insert figure 1 here'*

127 Melting tests on the homogeneous gneiss (NOP1) revealed that partial melting does not occur
128 for $T < 825^\circ\text{C}$ probably due to paucity of free water. Melting through the biotite – dehydration
129 reaction started for $T = 850^\circ\text{C}$. To avoid biotite melting and to promote melting through water
130 – present reactions and homogenous distribution of melt, the starting material was hydrated
131 prior to the deformation experiments. With the addition of free H_2O , experiments were run at
132 temperature of 750°C to avoid biotite – related melting.

133 Hydration was performed at room pressure and temperature during three days in a closed
134 glass containing distilled water. Complete and homogeneous hydration is only attained for
135 small core sizes (diameter = 5mm). To enhance hydration, cores were plunged into distilled
136 water and placed in a vacuum holder one hour per day. Hydrated cores were sealed within
137 gold caps and heated at 750°C , 300 MPa for 48 hours in an internal-heated vessel. In that
138 way, water was dissolved and trapped in the melt, which became hydrated glass when cores
139 were quenched. This hydrated homogeneous gneiss is sample NOP1-B whereas the dry
140 homogenous gneiss is sample NOP1-A (Table 1).

141 *'Insert Table 1'*

142

143 *2.2 Heterogeneous gneiss: sample PX28*

144 Starting material PX28 is a quartzo-feldspathic two – mica gneiss, sampled in the
145 Sioule Valley in the French Massif Central (46.110613, 3.013235). Modal composition is
146 50% quartz, 20% feldspars with mainly plagioclase and little K-feldspar, 20% biotite and
147 10% muscovite. Accessory minerals are zircon, apatite, and monazite. PX28 is well foliated

148 and shows a pronounced gneissic layering defined by millimetre – thick mica – rich and
149 quartz – rich layers (Fig. 1c). Within leucocratic layers, quartz and feldspars display a 50-100
150 μm grain size, with elongated biotite and few muscovite grains up to 100 μm long and 20 μm
151 thick. In mica-rich layers, biotites and muscovites are commonly 100-500 μm long and 10-50
152 μm thick and reach up to 1 mm long and 1 mm thick, with some very rare grains up to 3 mm
153 in length. Muscovite grains are preferentially located within mica – rich layers and represent
154 less than 1% of quartzo-feldspathic layers volume. Within mica – rich layers, foliation is
155 locally deflected by 100 μm to 1 mm thick shear zones (Fig. 1d) marked by mica deflections.
156 Within shear zones, some small 10-50 μm -size quartz and feldspar grains occur. One
157 experiment under hydrostatic conditions, i.e. without deformation, (PP123: 850°C, 300 MPa,
158 1h45 min; Table 1) was performed. Only slight modifications of PX28 fabric were observed
159 with quartz-feldspar grain boundaries becoming more rounded and production of melt. Within
160 shear zones, small grains became uncommon, which we attribute to melt consumption.
161 Deformation experiments were therefore preceded by a 30 minutes heating event under
162 hydrostatic conditions at running temperature so as to limit the influence of small – scale
163 structures and grain – size heterogeneities on melt generation and migration.

164

165 **3. Experimental methods**

166 Pure-shear deformation experiments were performed in an internally heated gas-
167 medium deformation apparatus (Paterson instrument, Australian Scientific Instrument) at
168 ISTO Orléans, France. Cylinders with 5 to 15 mm in diameter and 10.3 to 28.8 mm in length
169 (Table 1) are cored perpendicularly to the initial foliation for both natural gneisses. The
170 smallest diameter is used for experiments on the homogeneous gneiss NOP1 with water added
171 (starting material NOP1-B in Table 1) since complete hydration of a sample could only be
172 completed for the small – diameter cores. Length of cores depends on the fragility of the

173 material and/or the cylinder; as for example long cores with smallest diameter were difficult
174 to drill. Although cores of both gneisses have different mineral sizes and different diameters
175 of cylinder were used, a minimum of 30 grains could always be traversed across the core so
176 that individual large grains do not affect the mechanical behaviour of the entire samples.
177 Opposite faces of cylinders were finely polished to achieve parallelism within $\pm 3 \mu\text{m}$. Cores
178 were then inserted in a column assembly made of alumina and zirconia pistons enclosed in an
179 iron jacket (Champallier *et al.*, 2008). To limit loss of fluid and isolate the sample from the
180 thermocouple, two 3 mm-thick alumina spacers were inserted between the rock sample and
181 alumina pistons. Two geometries of column are used depending on core size. For the smallest
182 cores (diameter = 5 mm), a copper cylinder was introduced between the sample and the iron
183 jacket in order to fill the gap between them (cores: diameter = 5 mm, iron jacket: diameter =
184 10 mm). The diameter of the iron jacket was reduced to 10 mm at sample edges, forming
185 “dog-bone” geometry. For bigger cores, no reduction was needed since core diameter equals
186 internal iron jacket diameter. A platinum foil (25 μm) was systematically introduced between
187 core and iron jacket to prevent any chemical reaction between melt and iron. The column was
188 placed in the Paterson apparatus to locate the sample in the isothermal zone of the heating
189 chamber (temperature controlled at $\pm 1^\circ\text{C}$ over a distance of 5 cm). Temperature was
190 measured with a K-type thermocouple situated at 3 mm from the top of the sample. Argon
191 was used as confining medium. Force was applied with a motor located below the column
192 assembly, where the top of the column assembly being fixed. Force was monitored by an
193 internal load cell with a 10 N resolution (Champallier, 2005). Experiments were performed at
194 a constant 300 MPa confining pressure, at different temperatures (750°C, 850°C and 900°C)
195 and strain rates varying from 10^{-5} s^{-1} to $1.25 \cdot 10^{-3} \text{ s}^{-1}$. Experiment names are based on (1) type
196 of material, (2) temperature ($^\circ\text{C}$) and (3) glass content (surfacic %). For the homogeneous
197 gneiss (NOP1), experiments names start with “Ho” (Table 1). For the heterogeneous gneiss

198 (PX28), experiments names start with “He”. For example, Ho/750/6 corresponds to the
199 experiment performed on the homogeneous gneiss (NOP1) at 750°C with a glass content of
200 6%. Strain rate is kept constant over the whole duration of the Ho/750/6 experiment.
201 Ho/850/33, He/850/19 & He/900/21-32 experiments experienced several strain rate steps.
202 Details about experimental conditions are summarized in Table 1. Deformation began after
203 temperature and pressure equilibrium was reached, meaning that melting reactions or glass-to-
204 melt transformation began before deformation. Thus, deformation started in presence of melt.

205 The deformed cores were cut along the long axis, i.e. perpendicular to the protolith
206 foliation. Thin sections were observed under polarized microscope and SEM. Glass amount
207 after deformation was estimated from representative zones for each core (compilation of 4 to
208 15 SEM images). Given that glass and plagioclase have similar grey colour in SEM images,
209 which prevented automated calculation of glass amount. Glass location was optically
210 observed and manually drawn for each SEM image. To better resolve local glass (former
211 melt) distribution, chemical maps are also acquired at several locations for two representative
212 experiments (Ho/850/33 & He/900/21-32, see section 4.5). From the combination of
213 elemental maps, mineral phases are recognized by automatic clustering using “k-means”
214 algorithm. One pixel of each phase was manually picked as initial guess to ensure proper
215 convergence of the algorithm. The algorithm then assigns a phase to each pixel based on his
216 statistical similarity with those initial guess. Then pixels recognized as glass are counted to
217 calculate glass amount. Comparisons between manual and automatic estimations of glass
218 amount, on the same area, are in good agreement (e.g. for the zone represented in Fig. 11b:
219 22% obtained from manually drawn and 20% from computation).

220 Glass drawings together with SEM images were then analyzed by the intercept method
221 (Intercept2003 and SPO2003 software, Launeau & Robin, 1996; Launeau *et al.*, 2010), to
222 determine the statistical long-axis orientation of glass pockets and the amount (surfacic %) of

223 glass. Shear zones were optically recognized and shear zone geometry was drawn. Then shear
224 zone orientations were measured in the same way than glass (former melt) pockets.

225 For each protolith, two experiments were performed at two different temperatures to
226 achieve conditions with low and high melt fractions. Different strain rates varying from 10^{-5} s^{-1}
227 1 to $1.25 \cdot 10^{-3} \text{ s}^{-1}$ were tested, depending on the mechanical response of the sample during an
228 experiment.

229

230 **4. Experimental results**

231 *4.1 Partial melting reactions in both protoliths*

232 In non – deformed hydrated cores from the homogeneous gneiss NOP1 (after the
233 passage in an internal-heated vessel), glass is observed around muscovite grains in contact
234 with quartz (Fig. 2a) and contains small euhedral newly formed biotite and sillimanite. Rare
235 spinel and corundum are sometimes observed. These microcrystalline phases are
236 systematically oriented and do not show any typical quenching textures (disoriented acicular
237 growth pattern for instance). We therefore consider them as melting reaction products
238 together with the melt represented by the interstitial glass after quenching (Webb & Knoche,
239 1996). We interpret the presence of glass, biotite and sillimanite, between muscovite and
240 quartz, as indicating the water – present partial melting reaction documented in metapelitic
241 system (Clemens & Vielzeuf, 1987; Solar & Brown, 2001):



243 abbreviations after Kretz (1983). Spinel may be the product of the biotite – dehydration
244 reaction:



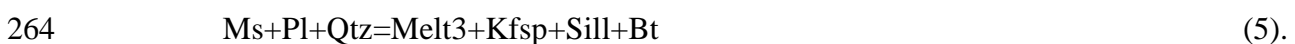
246 with sillimanite as a product of reaction (1). In the KFMASH system (rock chemistry reduced
247 to K, Fe, Mg, Al, Si and H a simplification relevant for quartzo-feldspathic rocks; Spear &
248 Cheney, 1989), spinel and corundum may result from the reaction:



250 In cores of NOP1-B, glass without any associated newly formed peritectic phase is also
251 abundant between plagioclase and quartz (same geometry than in Fig. 2b), indicating the
252 former presence of melt and thus the following water – present partial melting reaction
253 (Boettcher and Wyllie, 1969):



255 In cores from the heterogeneous gneiss PX28 and from non-modified homogeneous
256 gneiss NOP1 (NOP1-A in Table 1), the same glass and newly formed peritectic phases
257 association as in hydrostatic test experiments (e.g. PP123, Table 1) are observed. We
258 therefore interpret them as produced during the initial hydrostatic stage of the deformation
259 experiment. Glass is present around muscovite grains and along muscovite cleavages,
260 indicating the presence of former melt in contact of muscovite and quartz (Fig. 2c). Glass is
261 associated with newly formed peritectic grains (micrometric crystals with needle or prismatic
262 shape) of biotite, sillimanite and K-feldspar (Figs. 2c & d), indicating the following
263 dehydration partial melting reaction (Patiño Douce & Harris, 1998; Castro *et al.*, 2000):



265 Glass without newly formed peritectic phases is also observed at plagioclase-quartz grain
266 boundaries (Fig. 2b). Considering that temperatures and pressure used in those experiments
267 (850°C in He/850/19 and 900°C in He/900/21-32, both at 300 MPa) are too low for water –
268 absent partial melting of Plg+Qtz to occur (reaction reached at 900°C for similar pressure,
269 Boettcher and Wyllie, 1969), the former melt, now evidenced as glass, is interpreted as the

270 direct product of water – present partial melting (melt2 in reaction 4) or after interaction
271 between melt (melt3 formed by reaction 5) and plagioclase following the reaction:



273 For both protoliths, biotite also shows isolated glass pockets along cleavages (Fig. 2d).
274 This occurrence may indicate either sporadic hydrated partial melting of the biotite or
275 incipient destabilization of biotite within a former melt that was produced by reaction (1), (4)
276 or (5).

277 *'Insert figure 2 here'*

278

279 *4.2 Mechanical data*

280 *4.2.1 The homogeneous gneiss NOP1*

281 The two experiments on the homogeneous gneiss NOP1 were performed in different
282 manners: experiment Ho/750/6 was performed for one single strain rate value, whereas
283 experiment Ho/850/33 is the succession of four strain-rate steps, with an increase of strain
284 rate at each step. Even if protocols were different, it is possible to draw first order comparison
285 of stress evolution with strain between Ho/750/6 and the first step of Ho/850/33, both of them
286 being performed at strain-rates in the same order of magnitude ($5 \cdot 10^{-5} \text{ s}^{-1}$ and $2 \cdot 10^{-5} \text{ s}^{-1}$) and
287 both being deprived of any inheritance from earlier strain history. Experiment Ho/750/6
288 shows hardening with strain (Fig. 3a) whereas experiments Ho/850/33 first step reaches a
289 steady state (Fig. 3b). Experiment Ho/750/6 ($>200 \text{ MPa}$ at $2 \cdot 10^{-5} \text{ s}^{-1}$, Fig. 3a) reaches higher
290 stress than experiment Ho/850/33 ($<20 \text{ MPa}$ at $5 \cdot 10^{-5} \text{ s}^{-1}$; Fig 3b).

291

292 *4.2.2 The heterogeneous gneiss PX28*

293 At 10^{-4} s^{-1} , experiment He/850/19 reaches higher stress (circa 60 MPa Fig. 3c) than
294 experiments He/900/21-32 (ca. 10 MPa, Fig. 3d). The same observation is true for 10^{-3} s^{-1}

295 (>70 MPa in He/850/19 vs ca. 30 MPa in He/900/21-32; Figs. 3c & d). At 850°C in
296 He/850/19, the stress vs. strain curves show a stress peak at ca. 7% strain followed by the
297 very beginning of a strength decrease (Fig. 3c). At 900°C, in experiment He/900/21-32,
298 steady state is attained after ca. 10% strain with flow stresses about 10% of the confining
299 pressure at 10^{-3} s^{-1} (Fig. 3d).

300 *'Insert figure 3 here'*

301

302 *4.3 Microstructures at sample scale (1mm-1cm)*

303 *4.3.1 Microstructures in the homogeneous gneiss NOPI*

304 To a first order, the deformation distribution in both experiments (Ho/750/6 &
305 Ho/850/33) is mostly homogeneous given the near barrel shaped end-cores with smooth edges
306 and the lack of penetrative shear zones cross-cutting either sample (Fig. 4). In the low – glass
307 fraction experiment Ho/750/6, little strain localization is observed, as shear zones are rare and
308 small (only 8 observed) and connect to sample edges (Fig. 4a). Geometrically these shear
309 zones occur as planes with angles greater than 25° to the experimental compression direction
310 (black arrows in Fig. 4). However, the large range of angles and the small number of shear
311 zones prevent any statistical analysis. In high glass fraction experiment Ho/850/33, only five
312 shear zones are observed and they are all connected to sample boundaries without penetrating
313 more than a few mm into the sample (shear-zones reported in Fig. 4b were first observed on
314 SEM images).

315 *'Insert figure 4 here'*

316

317 *4.3.2 Microstructures in the heterogeneous gneiss PX28*

318 In the layered gneiss (PX28), deformation at core – scale is more heterogeneous as
319 primarily shown by the jagged edges of core samples (Fig. 5). In the experiment with low
320 glass content, run at 850°C (He/850/19), deformation is mainly accommodated by two core-
321 scale shear zones (in red in Fig. 5a). Deflection of the pre-existing foliation along the two
322 shear zones defines “shear zone boudins” as classified by Goscombe *et al.* (2004). Shear
323 zones orientations were systematically measured (angle to the experimental compression
324 direction) from image analysis and the minerals they affect systematically noted. We
325 distinguish mica-mica, mica-quartz, and quartz-quartz shear zones. Their offset being the
326 same order of magnitude or smaller than aggregate sizes, the association of minerals on each
327 side of shear zones is interpreted to be the shear zone initiation site. In He/850/19 experiment,
328 shear zones concentrate in or along mica – rich layers (Fig. 5a), as only two are observed
329 along quartz – quartz contacts (Fig. 6a). In experiment with the higher melt fraction,
330 conducted at 900°C (He/900/21-32), shear zones are distributed within or between micaceous
331 and quartzo-feldspathic layers (Figs. 5b & 6b).

332 *‘Insert figure 5 here’*

333 The average orientation of shear zones is close to 45° within both experiments (Fig.
334 6). In details, in He/850/19, shear zones lack an angle to experimental compression direction
335 less than 20°, and most angles are between 20° and 60° with a mean for the population of
336 about 45° (Fig. 6a). Shear zones with larger angles to the experimental compression direction
337 develop mainly in micas-rich layers. At 900°C and higher melt fraction (He/900/21-32), shear
338 zones have lower incidence values with a more pronounced peak in the 40-45° (Fig. 6b).

339 *‘Insert figure 6 here’*

340 In He/900/21-32, some quartz-feldspars layers are truncated into few millimetres-long
341 symmetric boudins while the mica – and glass – rich layers tend to occur within boudin-necks

342 (Figs. 5b & 7a). Here, boudins are mostly symmetrical with little slip along a single shear
343 band on the inter-boudin surface (no slip boudinage from Goscombe *et al.*, 2004).

344 *'Insert Figure 7 here'*

345

346 *4.4 Microstructures at grain-scale (μm - mm)*

347 *4.4.1 Microstructures in the homogeneous gneiss NOP1*

348 In Ho/750/6, mica grains were deformed by syn-experimental kink bands (Fig. 8a, red
349 lines in Fig. 4), whereas Ho/850/33 contains only a few kink bands. Some biotites with
350 sigmoid-like shapes are observed in both samples (Figs. 8c & d).

351 In experiment Ho/750/6, quartz grains are broken (“crystal breakage” in Fig. 4) and
352 the related inter-grain voids are generally empty, lacking glass (empty cracks in Fig. 8b). At
353 both temperatures (750 & 850°C), quartz grains may be completely broken into pieces of
354 different sizes, with each fragment being surrounded by glass, forming an interconnected
355 glass – filled fracture network (Figs. 8c, d and e). Such networks inside quartz grains have
356 larger expansion in Ho/850/33 (Fig. 8e) than in Ho/750/6 (Fig. 8c). In these networks, glass is
357 generally free of newly formed peritectic phases (Fig. 8e).

358 *'Insert figure 8 here'*

359

360 *4.4.2 Microstructures in the heterogeneous gneiss PX28*

361 A major difference between both experiments (He/850/19 & He/900/21-32) is that
362 muscovite is not observed anywhere in He/900/21-32, which means that muscovite completely
363 reacted during the experiment. As the only known reaction involving muscovite is
364 dehydration melting, we propose that muscovite entirely disappeared by dehydration melting.

365 In both experiments, biotites present sigmoid-like shapes (Fig. 7a). No kink-bands are

366 observed. Some biotites are broken in small pieces (<20 µm) and aligned along a plane that
367 we interpret as a shear zone (Fig. 7a). Biotites oriented perpendicularly to their initial
368 orientation and surrounded by glass, also containing newly formed peritectic phases, are
369 observed in He/900/21-32 (Fig. 7b), implying flow of biotite during deformation.

370 Newly formed peritectic phases are mainly observed in glass films along mica grains
371 and oriented parallel to the foliation. However in both experiments, changes in newly formed
372 peritectic phase orientation are observed along glass veins inside quartz grains (e.g. in
373 He/900/21-32 in Fig. 7c). This change in orientation of newly formed peritectic phases is
374 interpreted as marking flow of the peritectic phases-bearing melt.

375 Quartz grains show syn-deformation lobate boundaries and grain-size reduction (Figs.
376 9a & b), which are assumed to be due to partial consumption during melting reaction. Outside
377 of mica – rich layers, quartz and feldspar grains show offsets and relative displacements of
378 grains with respect to each other without evidence of cataclastic deformation of grains, nor
379 intracrystalline plasticity (Fig. 9c). The observation that glass fills all pores and boundaries
380 between the matrix grains supports a melt-assisted granular flow. Quartz and feldspar
381 breakage is observed in few locations (e.g. Fig. 7a), within shear zones. In He/900/21-32
382 experiment, very few glass-filled cracks within quartz and feldspar grains are observed (Fig.
383 7c).

384 *'Insert figure 9 here'*

385

386 *4.5 Glass distribution*

387 *4.5.1 Glass distribution in the homogeneous gneiss NOP1*

388 In experiments on the homogeneous gneiss (NOP1), glass content at 850°C is 5.5 time
389 greater than in experiment at 750°C (33% vs 6% respectively, Fig. 10 & Table 1). Glass is

390 located (1) at grain boundaries as 20-100 μ m thick films (Fig. 11b), (2) along micas cleavages
391 forming few μ m-size pockets (black arrows in Fig 11b) or (3) in quartz grains as injections
392 (blue triangles in Fig. 4; Fig. 11c). Glass injections, depleted in newly formed peritectic
393 minerals, are generally thicker at the boundary of their host grain or grain fragment (Figs. 8e
394 & Fig. 11c) and narrower within quartz grains, which allows determination of glass
395 movement direction, i.e. from mica grains toward quartz grain aggregates. Glass-filled cracks
396 within quartz-supported network (e.g. Figs. 8d & 11d) is systematically poor in newly formed
397 peritectic phases (in blue in Fig. 11d). Even if the zone illustrated in Fig. 11c is located
398 between two shear zones (thick dashed lines), its glass content is less than the zone in Fig.
399 11d, located away of any shear zone. The fact that shear zones do not correspond with high
400 glass fraction areas is observed over the whole sample (e.g. Figs. 8d & 10b) and in Ho/750/6.
401 No clear relation between glass distribution and shear zones localization can be identified
402 from sample examination.

403 In sample cores from both experiments, the main population of glass films and pockets
404 orientation is almost perpendicular to the experimental compression direction: 40% of the
405 glass pockets and films are between 80 and 120° in Ho/750/6, 26% in Ho/850/33 (Dark grey
406 population in rose diagrams in Fig. 10). A second population of glass orientations is present in
407 Ho/750/6 and is oblique to the experimental compression direction (Fig. 10a). In both
408 experiments, glass injections in quartz (glass location 3, see above) are sub-parallel to
409 experimental compression direction (light grey population in rose diagrams in Fig. 10).

410 *'Insert figures 10 and 11 here'*

411

412 *4.5.2 Glass distribution in the heterogeneous gneiss PX28*

413 In order to discuss glass distribution in heterogeneous gneiss PX28, several zones have
414 been carefully mapped as illustrated in Fig. 12. In He/850/19, one zone encompassing one

415 quartz-rich layer and one mica-rich layer have been delineated. Size of the zone (5mm x 5
416 mm) was determined so that enough grains were considered for statistical analysis of the rose
417 diagrams (more than 800 values for each). For He/900/21-32, two distinct zones were chosen.
418 One (Zone 1) is representative of the upper part of the core with alternations of 2 to 3 mm
419 thick, continuous quartz-rich layers with thinner continuous mica-rich layers. Zone 2 was
420 chosen to represent the lower part of the sample with disrupted mica-rich horizons within a
421 quartz-rich matrix. Once again, the size of each zone was determined so that enough grain
422 boundaries were mapped.

423 In experiments on the heterogeneous gneiss (PX28), mean glass content is $19\pm 6\%$ at
424 850°C (He/850/19) and ranges from 21 ± 7 to $32\pm 6\%$ at 900°C (He/900/21-32; Fig. 12 and
425 Table 1). Glass content has been measured across quartz – and mica – rich layers alternations
426 (Fig. 12). Glass content in mica – rich layers (22% in He/850/19, Fig. 12a, and 26% in
427 He/900/21-32, Fig. 12b) is systematically higher than in quartz-rich layers (13% in
428 He/850/19, Figure 12a, and 14% in He/900/21-32, Fig. 12b). At 850°C (in He/850/19), glass
429 is present around muscovite grains, which are still present. At 900°C (i.e. He/900/21-32),
430 muscovite is not observed anymore. Glass is present along and within biotite grains (Figs. 13b
431 & c). In quartz – rich layers, glass is mostly present at grain boundaries (Fig. 13c & d), but in
432 smaller amount than in mica – rich layers (13% in He/850/19 and 14% in He/900/21-32; Fig.
433 12). In He/900/21-32, glass is present in inter-boudin position within quartz – rich layers
434 (inter-boudin illustrated in Figs. 7a, 13b and located in Fig. 5), where local high glass-fraction
435 is reached (up to 41% in Fig. 13b). In both experiments, melt (observed as glass) is collected
436 within shear zones as illustrated by the example given in Fig. 7a. Glass is also present along
437 cracks in quartz or plagioclase (Figs. 7c & white arrows in 13c) and at quartz-plagioclase
438 grain boundaries (Fig. 13d). Newly formed peritectic phases are present in glass pockets or
439 glass films near micas (Fig. 13). Orientation of remaining micas flakes and solid reaction

440 products evidence that they were sucked toward dilatant sites like boudin-neck and shear
441 zones together with the moving melt (Figs. 7b, c & d). Heterogeneous distribution of glass is
442 documented in He/900/21-32. Fig. 12b shows two different zones that have different glass
443 fractions of $21\pm 7\%$ (zone 1) and $32\pm 6\%$ (zone 2). Zone 1 contains a 1 - 3 mm – thick quartz –
444 rich layer and is relatively poor in glass. Zone 2 contains more micaceous layers and shows a
445 greater glass content.

446 In both experiments considering the mica – rich and quartz – rich layers together, glass
447 areas have a strong preferred orientation normal to compression direction (rose diagrams in
448 Fig. 12). Nevertheless glass orientation varies between mica – rich and quartz – rich layers. In
449 He/850/19 (Fig. 12a), the dominant population of glass veins runs parallel to experimental
450 compression direction in quartz-rich layers (low angle bins in rose diagram), while dominant
451 population in mica-rich layers is perpendicular to experimental compression direction and
452 actually parallel to mica elongation axis. In He/900/21-32, orientation patterns are more
453 complex. Within the upper quartz layer of zone 1, a significant population of veins with low
454 angles to the experimental compression direction also appears (16% of all measured values),
455 while they are absent in the most mica-rich sub-layer despite representing 26% of all
456 measured values for the entire mica rich layer. In zone 2, glass is mainly oriented
457 perpendicularly to experimental compression direction (Fig. 12b).

458 *'Insert figures 12 and 13 here'*

459

460 **5. Discussion**

461 *5.1 Limits of this study*

462 Our aim is to investigate the effect of protolith initial texture and related incipient melt
463 distribution on melt flow during deformation. For this purpose, two sets of experiments on
464 two natural protoliths with particular experimental conditions were performed. Experimental

465 temperatures were chosen to get water – present and water – absent muscovite melting
466 reactions. A drawback of this approach to experimental temperature control is that these
467 changing conditions had an impact on melt viscosity that could not be measured in our
468 experiments. Nevertheless, published data about haplogranitic melts (Dingwell et al., 1996)
469 show that above 1 wt % H₂O and 700°C, impacts of temperature and hydration are limited
470 and effective viscosities are between 10⁷ and 10⁴ Pa.s, which is more than 6 orders of
471 magnitude below the effective viscosity of surrounding rock (10¹³ Pa.s for a dry Westerly
472 granite (Carter & Tsenn, 1987) strained at 1. 10⁵ s⁻¹ and 750°C).

473 Strain rate is another parameter that changes between experiments. The experiments with
474 different strain rate steps (Ho/850/33, He/850/19 & He/900/21-32) show that stress increases
475 with strain rate (Fig. 3). For instance, experiment Ho/850/33 exhibits an increase from 9.2 to
476 31 MPa when the strain rates increases from 1*10⁻⁵ to 1.25*10⁻³ s⁻¹. Stress is multiplied by 3.3
477 whereas strain rate is multiplied by 125, thus stress increase with strain rate remains limited.
478 Strain rates therefore seems to be a second-order.

479

480 *5.2 The meaning of glass locations and glass amounts*

481 Until now, we have been describing glass locations and amounts in our experiments.
482 However, our aim is to look at melt distribution and melt flow associated with deformation of
483 partially molten rocks. Thus, it is important to understand what “glass” represents. When
484 performing deformation, the temperature was higher than 750°C, which is far above the glass
485 to melt transition (Webb and Knoche, 1996). This state means that during deformation, melt
486 was present, and that the two gneisses were indeed partially molten. The transition from melt
487 to glass occurs at the end of the deformation event, when the oven is turned off leading to
488 rapid temperature decrease. Glass would therefore represent the melt, as usually considered
489 (e.g. Arzi, 1978; Misra *et al.*, 2009). Following this logic, glass locations and glass amount

490 represent melt locations and melt amounts, respectively. Thus, we will now speak of melt
491 instead of glass.

492

493 *5.3 Potential link between stress vs strain curves and microstructures*

494 Experiments on the homogeneous gneiss NOP1 show different stress vs. strain curves:
495 the low temperature and low melt-content experiment (Ho/750/6) shows hardening whereas
496 the experiment performed at higher temperature and melt content (Ho/850/33) shows steady
497 state at high finite strain (Fig. 3). Hardening behaviour was previously observed in
498 experiments for highly crystallized magma (crystal fractions larger than 0.5 and up to 0.8;
499 Arbaret *et al.*, 2007; Forien *et al.*, 2011). From these experiments performed in torsion, the
500 authors concluded that strain was mainly accommodated by the development of synthetic
501 normal Riedel – type shear zones that, associated with Trust – type shear bands, formed an
502 anastomosed network of shear zones delimitating lenses of less deformed melt-bearing zones.
503 In the shear zones, intragranular fracturing (i.e. crystal breakage) was identified (Arbaret *et*
504 *al.*, 2007). This crystal breakage is inferred to be related to intense stress at contact between
505 grains in localized zones submitted to large shear strains (Forien *et al.*, 2013). In addition,
506 they documented shear hardening in experiments where the crystals suffered intense
507 fracturing, whereas steady – state deformation occurred in experiments without any
508 generalized crystal breakage (Forien *et al.*, 2011). In our series of experiments on the
509 homogeneous gneiss NOP1, quartz – grain breakage (green dashed line in Fig. 4a and cracks
510 in Fig. 8b) is observed in Ho/750/6 while it is absent for the deformation experiment at higher
511 temperature with a larger melt fraction (Ho/850/33, Fig. 4b). Even if shear zones and crystal
512 breakage are less developed in Ho/750/6 than in the study of Forien *et al.* (2011), we conclude
513 that strain hardening behaviour of Ho/750/6 probably results from localized shear zones

514 together with regions of grain breakage that mainly accommodated the bulk sample
515 deformation.

516 Experiments on the heterogeneous gneiss PX28 also exhibit different behaviours (Fig.
517 3). He/900/21-32 experiment is characterized by stable low shear stress at large strains,
518 whereas He/850/19 seems to show a peak of high stress followed by the very beginning of
519 shear softening. A similar behaviour with shear softening following the high – stress peak was
520 experimentally reproduced in crystal-melt mixtures by Picard *et al.* (2011). They showed that
521 this behaviour was associated with the intense development of discrete Riedel shear zones
522 that localized the deformation. Numerous small shear zones are observed in He/900/21-32.
523 Based on this previous study, we conclude that the rheological behaviour exhibited by the
524 experiment He/850/19 is controlled by the early initiation of shear zones that subsequently
525 developed over the entire volume of the deformed core. In He/900/21-32, shear zones are less
526 developed and do not transect over the entire volume of the sample, so the strain-softening
527 behaviour is absent.

528 The difference between He/850/19 showing strain softening and He/900/21-32 showing a
529 steady state could also be explained by their difference in shear zone orientations.

530 Indeed, shear zones development and geometry are indicative of mechanical properties of the
531 studied aggregates (Veermer and De Borst, 1984; Veermer, 1990). Development of
532 compactant shear zones is expected to induce weakening of the overall material, while
533 dilatant shear zones are associated with bulk hardening (Veermer and De Borst, 1984).
534 Compactant (respectively dilatant) shear zones (with negative, respectively positive,
535 compaction angles) are expected to develop at angles higher (respectively lower) to σ_1
536 (equivalent to the experimental compression direction in our study) in the Roscoe model
537 (Veermer, 1990) considered as relevant for high confining pressures, as in our experiments
538 (Le Pourhiet, 2013). The observed distributions could reflect this contrast with shear zones

539 developing at higher angle in He/850/19 than in He/900/21-32. Their distribution in quartz –
540 or mica – rich layer could also explain these differences. In He/900/21-32, most low-angle
541 shear zones were measured in quartz layers, while high-angle shear zones were mostly
542 measured in mica – rich layers in both He/900/21-32 and He/850/19 experiments. Within the
543 layered gneiss, melt produced by mica partial melting is present in greater amounts in mica-
544 rich layers, indicating that partial melting occurred preferentially in mica – rich layers. In
545 addition, microstructural observations show that melt primarily located in the sheared
546 micaceous layers flowed toward the quartz-feldspatic layers and filled the low-angle shear
547 zones. Thus, one could consider that shear zones developing in mica – rich layers release
548 melt, and therefore are compactant, while shear zones developing in quartz – rich layers trap
549 melt, and therefore dilate. In He/900/21-32, development of dilatant shear zones in quartz and
550 compactant shear zones in mica promote drainage of melts from mica – rich layers to quartz –
551 rich layers without significant weakening, while in He/850/19, shear zones in mica – rich
552 layers prevail and anastomose in a sample-scale compacting shear zone inducing overall
553 weakening.

554

555 *5.4 Impacts of gneissic layering on melt flow*

556 Melt distribution within partially molten rocks first reflects the initial distribution of
557 melt production sites. In our experiments, we focused on water – present and muscovite –
558 dehydration melting reactions to test the change in melt distribution during deformation of
559 two kinds of partially molten rocks: one rock with incipient melt homogeneously distributed
560 (NOP1) and one with a heterogeneous melt distribution that mimics gneissic layering of the
561 protolith (PX28).

562 In the case of the homogeneous gneiss NOP1, sites of melt production are directly
563 related to muscovite locations. Muscovite is homogeneously distributed at sample scale,

564 which means that in both experiments (Ho/750/6 & Ho/850/33) melt is produced all over the
565 sample. This interpretation is corroborated by the fact that melt contents calculated in
566 different locations are equal at the sample scale. Results of the experiments performed on the
567 homogeneous migmatite show that melt movement is limited to melt – filled injections in
568 quartz grains at μm -scale and melt does not flow from initiation sites into possible pathways
569 such as shear zones. Shear zones are observed in the deformed homogeneous gneiss (Fig. 4).
570 However, they do not correspond with high melt areas, implying that they do not concentrate
571 melt, which means that melt did not move toward shear zones. The lack of melt movement
572 may be explained by (1) limited melt – pressure gradients within the sample, (2) limited
573 connectivity of the melt or (3) a high melt viscosity. A high viscosity may be rejected because
574 the melt was hydrated, which means that its viscosity is low (Shawn, 1965). Melt connectivity
575 could not be estimated in this study. However, previous studies on hydrated partially molten
576 granite or aplite, i.e. two homogeneous rocks, show that melt is connected as soon as 7% melt
577 is present (see in Rosenberg and Handy, 2005). Mean melt content in Ho/750/6 is really close
578 to 7% (Table 1), even if it may be less locally. Thus, melt connectivity is likely to have
579 occurred, at least in some portions of the sample volume. However, melt connectivity is not
580 sufficient to promote melt flow. A driving force is needed. Therefore, limited melt transport
581 more probably relates to limited melt – pressure gradient within the sample. As melt is
582 produced homogeneously at sample scale, there is no melt concentration gradient and thus no
583 melt pressure gradient is created. The lack of melt – pressure gradient probably prevents melt
584 movement. Thus, the melt distribution in the homogeneous gneiss NOP1 is mainly controlled
585 by the location of melting reactants, which is controlled by the initial protolith fabric and the
586 initial spatial distributions of the grains for the different mineral components (known for static
587 conditions, Mehnert *et al.*, 1973).

588 In contrast, melt is heterogeneously distributed in experiments on the heterogeneous
589 gneiss PX28 (He/850/19 & He/900/21-32). Evidences of strong melt flow as exemplified by
590 strong alignment of peritectic minerals and the presence of melt+peritectic minerals in shear
591 zones and interboudin positions are observed for the deformed layered migmatite (PX28; Fig.
592 7). In these experimentally deformed rock samples, gneissic layering strongly enhanced the
593 production and coalescence of melt along mica – rich layers. This enhancement causes a
594 strong pressure gradient between the two compositionally different layers, i.e. between mica –
595 rich and quartz – rich layers. This heterogeneous distribution of melt increases the strength
596 difference and enhances deformation partitioning between mica – rich and quartz – rich
597 layers. This contributes to localizing deformation along shear zones and boudin-necks acting
598 as low melt – pressure sites into which melt migrates efficiently.

599

600 *5.5 Comparison with natural migmatites*

601 In nature, incipient partial melting leads to the formation of metatexite, where
602 paleosome dominates, and where crystallized melt appears as leucosomes arranged as
603 elongated pockets that parallel the protolith planar fabric (Fig. 14). A similar pattern of melt
604 distribution parallel to protolith foliation is observed in our experiments for both homogenous
605 and heterogeneous starting materials but with differences in melt flow during experiment. We
606 propose that the particular orientation of melt perpendicular to the compression direction
607 reflects a strong control of the initial orientation of reactants. This hypothesis is compatible
608 with the process of microstructure development proposed by Holyoke and Rushmer (2002),
609 (Figs. 13 and 14 in Holyoke and Rushmer, 2002)

610 In the case of the homogeneous gneiss NOP1, melt distribution is not disturbed by
611 deformation and melt does not migrate. Melt remains located in films perpendicular to
612 shortening direction (Figs. 10 & 12), as already observed by Holyoke & Rushmer (2002),

613 which is opposite to results from numerous previous studies where melt concentrates within
614 cracks and grain boundaries that are parallel to the shortening direction (e.g. van der Molen &
615 Paterson, 1979; Rutter & Neumann, 1995).

616 For the heterogeneous migmatite (PX28), the early melt distribution is modified
617 during deformation and subsequent melt migration. Shearing along melt-bearing micaceous
618 layers, shear bands development and boudinage provide efficient pathways for melt
619 migration. The co-location of melt products with such positions is observed within natural
620 migmatites where due to competency contrast between various layers, leucosome is located in
621 dilatant structural sites, such as the spaces between boudins, in pressure shadows, or in
622 fractures in the more competent layers of migmatites (Figs. 14b, c). Occurrences of
623 leucosomes, which derived from crystallized melt, at the neck of boudins are described in
624 numerous terrains (e.g. Port Navalo French Armorican Massif: Marchildon & Brown, 2003;
625 British Columbia: Sawyer, 2008; Western Gneiss Region Norway: Ganzhorn *et al.*, 2014) and
626 may be compared to melt flow observed in experiments on the heterogeneous gneiss PX28,
627 even if the scales are different. Shear zones and more particularly the ones that transect mica-
628 rich and quartz-rich layers, build connection between high-pressure and low-pressure zones,
629 and thus, enhance melt flow as observed in nature with crosscutting leucosomes feeding
630 granite dyke networks.

631

632 6. Conclusion

633 Comparison of pure-shear experiments on a homogeneous gneiss and a heterogeneous
634 layered gneiss shows that initial compositional layering of the protolith have a great influence
635 on melt distribution and melt flow. In the homogeneous gneiss, the main result is the lack of
636 melt migration toward melt collection zones during deformation experiments. In contrast,
637 experiments on the strongly layered gneiss show deformation partitioning between mica –

638 rich and quartz – rich layers, creation of interconnected pathways that drain and collect melt
639 efficiently. The presence of gneissic layering with the alternation of fertile and non-fertile
640 layers enhances melt – pressure gradients, deformation partitioning with boudinage and shear
641 zone development, driving melt flow through the partially-molten rock. Consequently melt
642 flow within a metatexite is greatly enhanced if the protolith of the partially molten rock shows
643 an inherited gneissic layering.

644

645 **Acknowledgment**

646 We thank C. Teyssier and an anonymous reviewer for thorough reviews and W.
647 Dunne for his attentive care and helpful review. This study benefited from discussions and
648 has received funding from the European Research Council (ERC) under the seventh
649 Framework Program of the European Union (ERC Advanced Grant, grant agreement No
650 290864).

651

652 **References**

- 653 Arbaret, L., Bystricky, M., Champallier, R., 2007. Microstructures and rheology of hydrous
654 synthetic magmatic suspensions deformed in torsion at high pressure. *Journal of*
655 *Geophysical Research*, 112, B10208.
- 656 Arzi, A.A., 1978. Critical phenomena in the rheology of partially melted rocks. Brown, M., &
657 Solar, G.S, 1998, Granite ascent and emplacement during contractional deformation in
658 convergent orogens. *Journal of Structural Geology*, v20, 9-10, 1365-1393.
- 659 Boettcher, A.L., Wyllie, P.J., 1969. Phase relationships in the system NaAlSiO₄-SiO₂-H₂O
660 to 35 kilobars pressure. *American Journal of Science*, 267, 875-909.

661 Brown, M., Solar, G.S., 1998. Granite ascent and emplacement during contractional
662 deformation in convergent orogens. *Journal of Structural Geology*, 20, 1365-1393.

663 Cadwell, W.B., Klemperer, S.L., Rai, S.S., Lawrence, J.F., 2009. Partial melt in the upper-
664 middle crust of the northwest Himalaya revealed by Rayleigh wave dispersion.
665 *Tectonophysics*, 477, 58-65.

666 Castro, A., Guillermo Corretgé, L., El-Biad, M., El-Hmidi, H., Fernandez, C., Patiño-Douce,
667 A.E., 2000. Experimental Constraints on Hercynian Anatexis in the Iberian Massif,
668 Spain. *Journal of Petrology*, 41, 10, 1471-1488.

669 Carter, N.L., Tsenn, M.C., 1987. Flow properties of continental crust. *Tectonophysics*, 136,
670 27-63.

671 Champallier, R., 2005. Déformation expérimentale à Haute Température et Haute Pression de
672 magmas partiellement cristallisés. 213 p.

673 Champallier, R., Bystricky, M., Arbaret, L., 2008. Experimental investigation of magma
674 rheology at 300 MPa: from pure hydrous melt to 76 vol.% of crystals. *Earth and*
675 *Planetary Science Letters*, 267, 3-4, 571-583.

676 Clemens, J.D., Vielzeuf, D., 1987. Constraints on melting and magma production in the crust.
677 *Earth and Planetary Science Letters*, 86, 2-4, 1987.

678 Cooper, R.F., Kohlstedt, D.L., 1984. Solution-precipitation enhanced diffusional creep of
679 partially molten olivine-basalt aggregates during hot-pressing. *Tectonophysics*, 107,
680 207-233.

681 Daines, M.J., Kohlstedt, D.L., 1997. Influence of deformation on melt topology in peridotites.
682 *Journal of Geophysical Research: Solid Earth*, 102, 10257-10271.

683 Dingwell, D.B., Romano, C., Hess, K.V., 1996. The effect of water on the viscosity of a
684 haplogranitic melt under PTX conditions relevant for silicic volcanism. *Contributions to*
685 *Mineralogy and Petrology*, 124, 19-28.

686 Forien M., Arbaret L., Burgisser A., Champallier R., 2011. Crystal breakage in magmas:
687 experimental constrains. *Journal of Geophysical Research*, 116,
688 doi:10.1029/2010JB008026.

689 Ganzhorn, A.C., Labrousse, L., Prouteau, G., Leroy, C., Vrijmoed, J., Andersen, T.B.,
690 Arbaret, L., 2014. Structural, petrological and chemical analysis of syn-kinematic
691 migmatites: insights from the Western Gneiss Region, Norway. *Journal of Metamorphic*
692 *Geology*, 32, 647-673.

693 Goscombe, B.D., Passchier, C.W., Hand, M., 2004. Boudinage classification: end-member
694 boudin types and modified boudin structures. *Journal of Structural Geology*, 26, 739-
695 763.

696 Hashim L., Gaillard F., Champallier R., Le Breton N., Arbaret L., Scaillet B., 2013.
697 Experimental assessment of the relationships between electrical resistivity, crustal
698 melting and strain localisation beneath the Himalayan-Tibetan belt. *Earth and Planetary*
699 *Science Letter*, 373, 20-30

700 Holyoke III, C.W., Rushmer, T., 2002. An experimental study of grain scale melt segregation
701 mechanisms in two common crustal rock types. *Journal of Metamorphic Geology*, 20, 5,
702 493-512.

703 Kretz, R., 1983. Symbols for rock-forming minerals. *American Mineralogist*, 68, 277-279.

704 Kohlstedt, D.L., Zimmerman, M.E., 1996. Rheology of partially molten mantle rocks. *Annual*
705 *Review of Earth and Planetary Sciences*, 24, 41-62.

706 Labrousse, L., Prouteau, G., Ganzhorn, A.C., 2011. Continental exhumation triggered by
707 partial melting at ultra-high-pressure. *Geology*, 39, 1171-1174.

708 Laporte, D., Watson, E. B., 1995. Experimental and theoretical constraints on melt
709 distribution in crustal sources: the effect of crystalline anisotropy on melt
710 interconnectivity. *Chemical Geology*, 124, 161-184.

711 Launeau, P., Robin P.-Y., 1996. Fabric analysis using the intercept method. *Tectonophysics*,
712 267, 1-4, 91-119.

713 Launeau, P., Archanjo, C.J., Picard, D., Arbaret, L., Robin, P.-Y., 2010. Two- and three-
714 dimensional shape fabric analysis by the intercept method in grey levels.
715 *Tectonophysics*, 492, 1-4, 230-239.

716 Le Pourhiet, L., 2013. Strain localization due to structural softening during pressure sensitive
717 rate independent yielding. *Bulletin de la Société Géologique de France*, 184, 4-5, 357–
718 371.

719 Marchildon, N., Brown, M., 2003. Spatial distribution of melt-bearing structures in anatectic
720 rocks from Southern Brittany, France: implications for melt transfer at grain- to orogen-
721 scale. *Tectonophysics*, 364, 3-4, 215-235.

722 Mehnert, K.R., Büsch, W., Schneider, G., 1973. Initial melting at grain boundaries of quartz
723 and feldspar in gneisses and granulites. *Neues Jahrbuch des Mineralogie Monatshefte*,
724 165-183.

725 Misra, S., Burlini, L., Burg, J.P., 2009. Strain localization and melt segregation in deforming
726 metapelites. *Physics of the Earth and Planetary Interiors*, 177, 173-179.

727 Misra, S., Burg, J.P., Mainprice, D., Vigneresse, J.-L., 2014. Rheological transition during
728 large strain deformation of melting and crystallizing metapelites. *Journal of*
729 *Geophysical Research – Solid Earth* 119, doi:10.1002/2013JB010777.

730 Nelson, K. D., Zhao, Wenjin, Brown, L. D., Kuo, J., Che, Jinkai, Liu, Xianwen, Klemperer,
731 S. L., Makovsky, Y., Meissner, R., Mechie, J., Kind, R., Wenzel, F., Ni, J., Nabelek, J.,
732 Leshou, Chen, Tan, Handong, Wei, Wenbo, Jones, A. G., Booker, J., Unsworth, M.,
733 Kidd, W. S. F., Hauck, M., Alsdorf, D., Ross, A., Cogan, M., Wu, Changde, Sandvol,
734 E., Edwards, M., 1996. Partially Molten Middle Crust Beneath Southern Tibet:
735 Synthesis of Project INDEPT Results. *Science*, 1684-1688.

736 Patiño Douce, A.E., Harris, N., 1998. Experimental Constraints on Himalayan Anatexis.
737 *Journal of Petrology*, 39, 4, 689-710.

738 Picard, D., Arbaret, L., Pichavant, M., Champallier, R., Launeau, P., 2011. Rheology and
739 microstructure of experimentally deformed plagioclase suspensions. *Geology*, 39, 747-
740 750.

741 Rosenberg, C.L., Handy, M.R., 2005. Experimental deformation of partially melted granite
742 revisited: implications for the continental crust. *Journal of Metamorphic Geology*, 23,
743 19-28.

744 Rudnik, R.L., 1995. Making continental crust. *Nature*, 378, 571-578.

745 Rutter, E.H., Neumann, D.H.K., 1995. Experimental deformation of partially molten Westerly
746 granite under fluid-absent conditions, with implications for the extraction of granitic
747 magmas. *Journal of Geophysical Research*, 100, 15,697-15,715.

748 Rutter, E.H., Brodie, K.H., Irving, D.H., 2006. Flow of synthetic, wet, partially molten
749 « granite » under undrained conditions: An experimental study. *Journal of Geophysical*
750 *research*, 111, B06407.

751 Sawyer, E.W., 2008. Atlas of Migmatites. *The Canadian Mineralogist Special Publication*, 9,
752 371.

753 Shawn, H.R., 1965. Comments on viscosity, crystal setting, and convection in granitic
754 magmas. *American Journal of Science*, 263, 120-152.

755 Solar, G.S., Brown, M., 2001. Petrogenesis of Migmatites in Maine, USA: Possible Source of
756 Peraluminous Leucogranite in Plutons? *Journal of Petrology*, 42, 4, 789-823.

757 Spear, F.S., Cheney, J.T., 1989. A petrogenitic grid for pelitic schists in the system SiO_2 -
758 Al_2O_3 - FeO - MgO - K_2O - H_2O . *Contributions to Mineralogy and Petrology*, 101, 149-164.

759 Trap, P., Faure, M., Lin, W., Augier, R., Fouassir, A., 2011. Syn-collisional channel flow and
760 exhumation of Paleoproterozoic high pressure rocks in the Trans-North China Orogen:
761 the critical role of partial melting and orogenic bending. *Gondwana Research*, 20, 498-
762 515.

763 Turmakina, E., Misra, S., Burlini, L., Connolly, J.A.D., 2011. An experimental study of the
764 role of shear deformation on partial melting of a synthetic metapelite. *Tectonophysics*,
765 503, 92-99.

766 van Der Molen, I., Paterson, M.S., 1979. Experimental deformation of partially melted
767 granite. *Contributions to Mineralogy and Petrology*, 70, 299-318.

768 Vermeer, P.A., De Borst, R., 1984. Non-Associated Plasticity for Soils, Concrete and Rock.
769 *HERON*, 29, 1984.

770 Vermeer, P.A., 1990. The orientation of shear bands in biaxial tests. *Geotechnique*, 40, 223-
771 236.

772 Webb, S., Knoche, R., 1996. The glass-transition, structural relaxation and shear viscosity of
773 silicate melts. *Chemical Geology*, 128, 165-183.

774 Zimmerman, M. E., Zhang, S., Kohlstedt, D. L., & Karato, S. I., 1999. Melt distribution in
775 mantle rocks deformed in shear. *Geophysical Research Letters*, 26, 1505-1508.

776

777

778

779 **Figure Captions**

780

781 Figure 1: Initial structure of the two starting materials: the homogeneous gneiss NOP1 (a, b)
782 and the heterogeneous gneiss PX28 (c, d). a) Cross-polarized image of NOP1 thin section
783 showing the homogeneous distribution of phases. b) Grain size differences between quartz
784 aggregates and plagioclase+mica aggregates in NOP1 (cross-polarized image). c) Cross-
785 polarized image of thin section showing mineral layering in PX28. d) Mica-rich layer
786 showing shear-zones in PX28. Pl: plagioclase, Qtz: quartz, Bt: biotite, Ms: Muscovite.

787

788 Figure 2: SEM images of textures related to partial melting reactions. a) Glass between
789 muscovite and quartz in hydrated undeformed homogeneous gneiss NOP1 (NOP1-B in Table
790 1), indicating water – present partial melting. b) Glass between quartz and plagioclase
791 indicating the following water – present partial melting reaction: $plg+qtz+H_2O=Melt$. The
792 same geometry is observed in cores from NOP1. c) Glass between muscovite and quartz in
793 the experiment at 900°C on the heterogeneous gneiss, indicating the muscovite – dehydration
794 partial melting. A similar reaction occurs in NOP1 (NOP1-A). d) Newly-formed peritectic
795 phase flow around biotite. Pl: Plagioclase, Ms: muscovite, Bt: biotite, Qtz: quartz, Gl: glass.

796

797 Figure 3: Stress vs. strain curves for both sets of experiments. Numbers labelled on curves are
798 strain rates.

799

800 Figure 4: Sample-scale deformation in the homogeneous gneiss NOP1 at 750°C (a) and
801 850°C (b). Black arrows: the experimental compression direction. Dashed line rectangles:
802 Locations for SEM images from Fig. 8.

803

804 Figure 5: Sample - scale deformation in the heterogeneous gneiss PX28 at 850°C (a) and
805 900°C (b). For each experiment: left: SEM image, middle: photo of the thin-section, right:
806 drawing indicating the main deformation structures. a) He/850/19 experiment showing two
807 sample-scale shear zones. b) He/900/21-32 experiment showing local shear zones and
808 boudinage of quartz – rich layer. Red lines associated to arrows: local shear zones. Black
809 arrows: the experimental compression direction. Dashed line rectangles: Locations for SEM
810 images from Fig. 7.

811

812 Figure 6: Shear zone orientations in experiments on the heterogeneous gneiss PX28. N:
813 number of shear zone used in the diagram. Mean: average orientation of shear zones. Colour
814 corresponds to the location of shear zone in regards to adjacent grains (e.g. quartz/quartz
815 means that the shear zone is between quartz grains). σ_1 : experimental compression direction.

816

817 Figure 7: Grain-scale deformation in experiments on the heterogeneous gneiss PX28. a)
818 Biotite showing a sigmoid-like shape and broken biotites aligned along a plan representing a
819 shear zone. Location in Fig. 5a. b) Biotite and newly formed peritectic phase flow with glass
820 in quartz – rich layer at the location of boudinage (see Fig. 5b). d) Change in newly formed
821 peritectic phases orientation indicating flow of glass and peritectic phases. F_i : initial
822 orientation (corresponding to the foliation) of newly formed peritectic phases. c) Glass with
823 newly formed peritectic phase along cracks in plagioclase grains. All newly formed peritectic
824 phases are oriented parallel to crack walls. The light grey phase in contact between glass and
825 plagioclase is a K-rich phase, which may be due to reaction between glass and plagioclase.

826 Bt: biotite, Qtz: quartz, Gl: glass, Pl: plagioclase, Kfsp: K-feldspar.

827 Figure 8: Grain – scale deformations in experiments on the homogeneous gneiss NOP1. a)
828 Kink bands in micas. Dashed lines: axial plan of kink bands. b) Empty cracks in quartz grain.
829 The curved crack along a glass filled crack is due to decompression. c) & d) Glass filled
830 fracture network in quartz grains. c) White dashed lines: contours of glass filled fracture
831 network. Red dashed line: shear zone. d) Arrows: glass filled fracture network in quartz. e)
832 Glass filled injections. Dash lines highlight injections shape. Locations of b), c), d) and e) are
833 given in Fig. 4. Ms: muscovite. Bt: biotite, Gl: glass, Qtz: quartz, Pl: plagioclase.

834

835 Figure 9: a) Photomicrograph showing lobate grain boundaries along quartz grains in contact
836 with glass (Gl). b) SEM image showing lobate boundaries along quartz grains in contact with
837 glass. c) Photomicrograph and related schematic drawing (d) showing melt distribution along
838 quartz grain boundaries and intergranular displacements of quartz grains with respect to each
839 other. This might argue for melt assisted granular flow.

840

841 Figure 10: Glass distribution in experiments on the homogeneous gneiss NOP1. Glass is
842 represented in black in the drawings. The rose-diagrams represent glass film or pocket
843 orientations. Dark grey population: glass films and pockets perpendicularly oriented to the
844 experimental compression direction (black arrows). Light grey: orientation population
845 corresponding to glass injection. The second population in a) corresponds to melt films and
846 pockets with an oblique orientation to the experimental compression direction. Dashed red
847 lines in b): shear zones (corresponding to the ones in Fig. 8d) showing no increase in melt
848 content at their vicinity.

849

850 Figure 11: Local glass distribution in Ho/850/33. a) Location of b, c, and d in Ho/850/33 core.
851 Location of Fig. 10b is also reported. Thick black dashed lines: shear zones defined from Fig.

852 4b. b) Glass associated to micas. White arrows: glass films along muscovite – quartz
853 boundaries often associated with newly formed peritectic phases (blue). Glass with newly
854 formed peritectic phases is only found close to micas. Black arrows: glass always associated
855 to newly formed peritectic phases along mica cleavage. c) Glass filled crack (white arrow)
856 parallel to the experimental compression direction (black arrows) in quartz grain. Thin dashed
857 black lines mark the shape of the crack. Thick oblique dashed lines: shear zones defined from
858 Fig. 4b. Glass in not particularly accumulates at the vicinity of shear zones. d) Glass filled
859 cracks free of newly formed phase in quartz supported network.

860 Glass estimates correspond to blue and red colours. ϕ : newly formed peritectic phases. Thick
861 vertical black arrows: experimental compression direction. Bt: biotite, Ms: muscovite, Gl:
862 glass, Kfs: K-feldspar, Pl: plagioclase, Qtz: quartz. Other: accessory minerals and K-rich
863 phase in contact between plagioclase and melt.

864

865 Figure 12: Glass distribution in experiments on the heterogeneous gneiss PX28. Glass is
866 represented in black in the drawings. The rose-diagrams represent glass film or pocket
867 orientations. a) Greater glass amount in mica – rich layer than in quartz – rich layer. Glass
868 films and pockets oriented perpendicularly to the experimental compression direction (black
869 arrows) in mica – rich layer and parallel to the experimental compression direction in quartz –
870 rich layer. b) High variability of glass amount at sample scale and between mica – rich and
871 quartz – rich layers. Black arrows=experimental compression direction.

872

873 Figure 13: Local glass distribution in He/900/21-32. a) Location of the different areas
874 illustrated in b), c) and d). b) Great glass amount associated with newly formed peritectic
875 phases and small biotites in an inter-boudin position (defined in Fig. 5b). Green dashed lines
876 in a) and b) correspond to the boundary of inter-boudin area as defined in Fig. 5b. c) Glass

877 veins, free of newly formed phase, in quartz grain (white arrow). Glass is also present within
878 plagioclase grain. d) Glass films, free of newly formed peritectic phase, at quartz –
879 plagioclase boundaries.

880 Glass estimates correspond to blue and red colours. ϕ : newly formed peritectic phases. Other:
881 accessory minerals and K-rich phase in contact between plagioclase and melt. Bt: biotite, Ms:
882 muscovite, Gl: glass, Kfs: K-feldspar, Pl: plagioclase, Qtz: quartz.

883

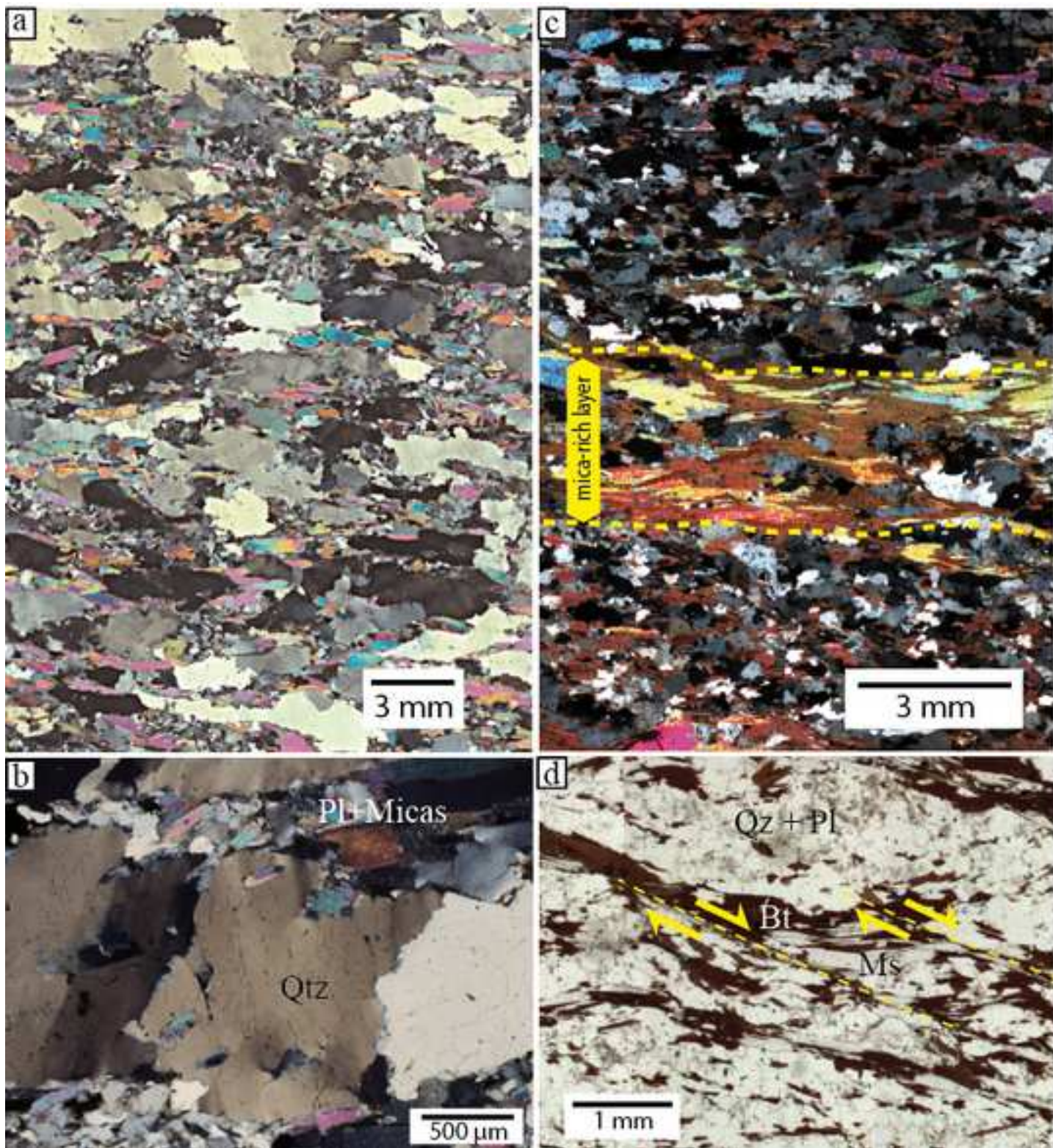
884 Figure 14: a) Outcrop photograph showing a metatexite where the onset of partial melting is
885 marked by ca. 20 cm long lense-shaped leucosomes that lie parallel to the planar fabrics of the
886 protolith, Fuping complex (North China Craton). b) Stromatic metatexite of paragneiss where
887 boudinage of quartz-rich competent layers led to melt migration toward boudin-neck (white
888 arrows), southern Velay dome (French Massif Central, France).c) Stromatic migmatite with a
889 set of leucosomes that parallels the gneissic layering and a second set of leucosomes located
890 in shear zones. Melt migrates toward shear zones, Archean Snowbird tectonic zone (Canada,
891 courtesy from Philippe Goncalves).

892

893 **Table caption**

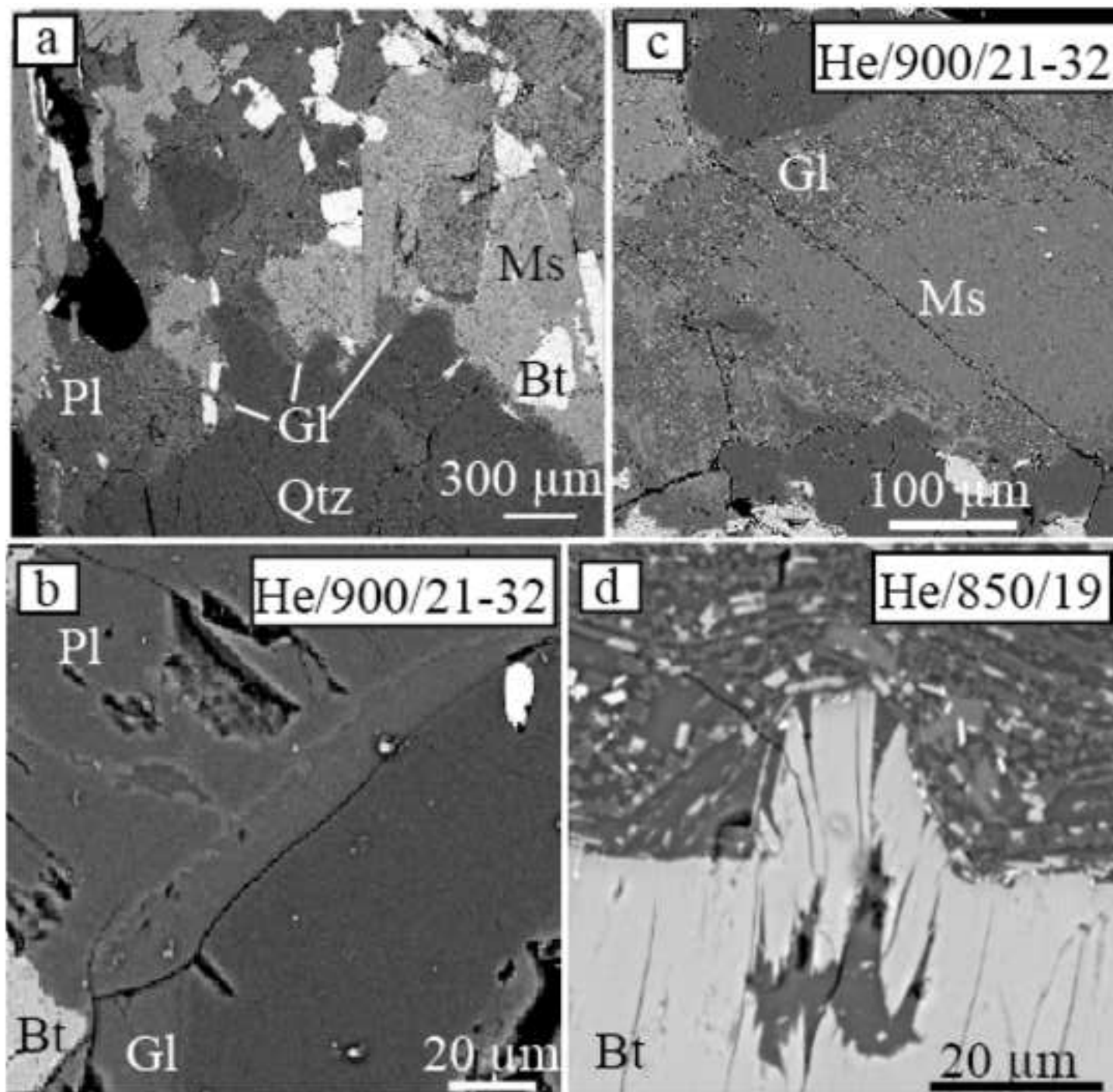
894 Table 1: Experimental conditions used in deformation experiments and parameters derived
895 from the experiments. PP123 is a hydrostatic experiment. Experiment names are built on the
896 following schema: “type of material/temperature (°C)/melt content (surfacic percentage)”.
897 “Ho” means homogeneous gneiss and “He” means heterogeneous gneiss. In the particular
898 case of He/900/21-32, it is not possible to define a meaningful mean main content as melt
899 content varies a lot through the sample (see Fig. 12). Thus we use both estimates made in two
900 different zones (see part 4.5).

*Figure1
[Click here to download high resolution image](#)



*Figure2

[Click here to download high resolution image](#)



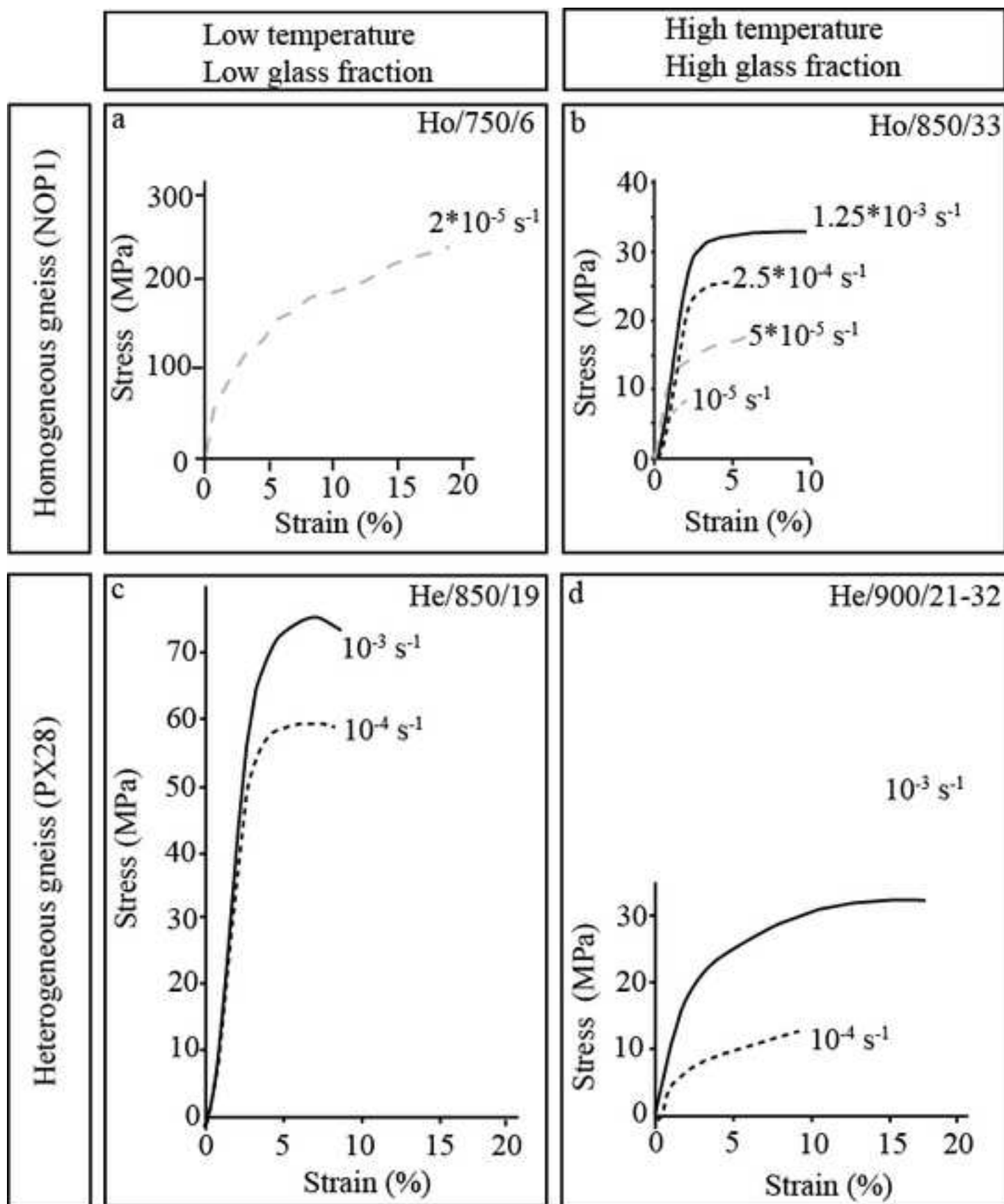
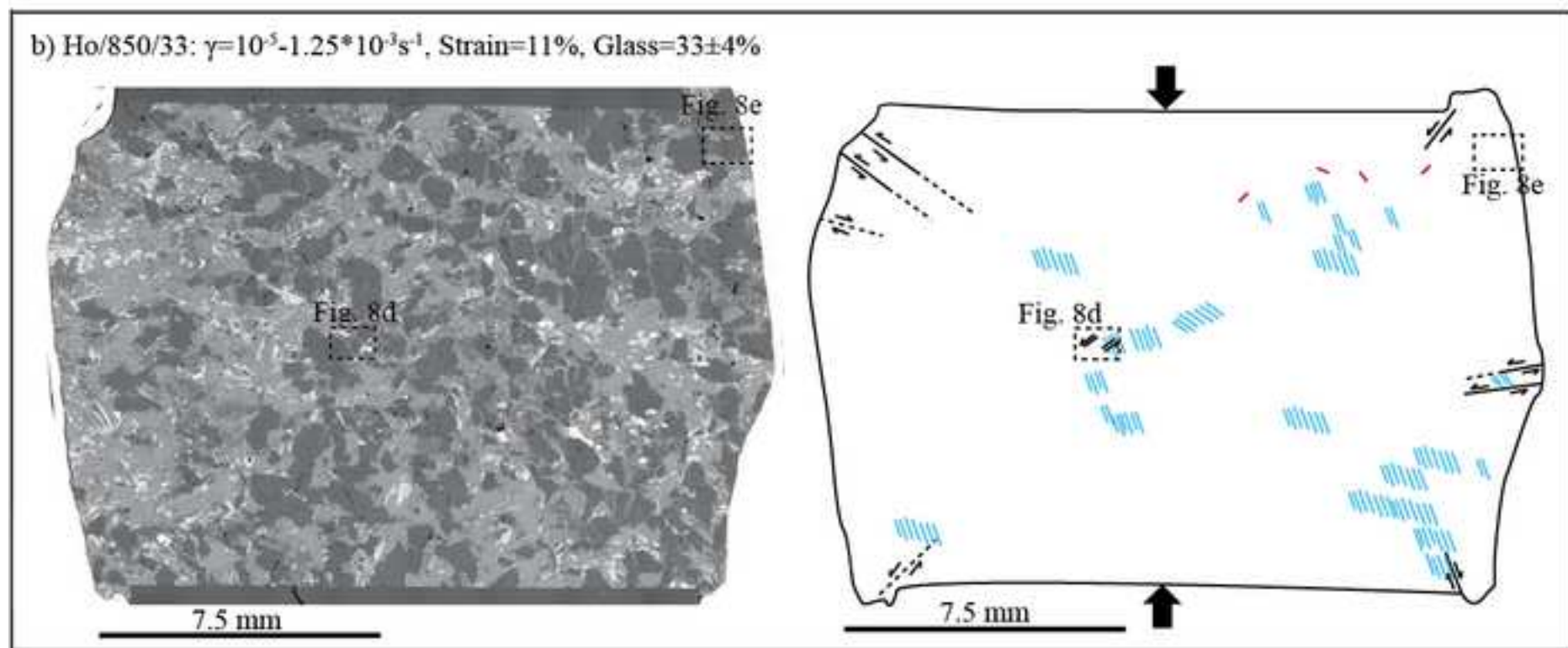
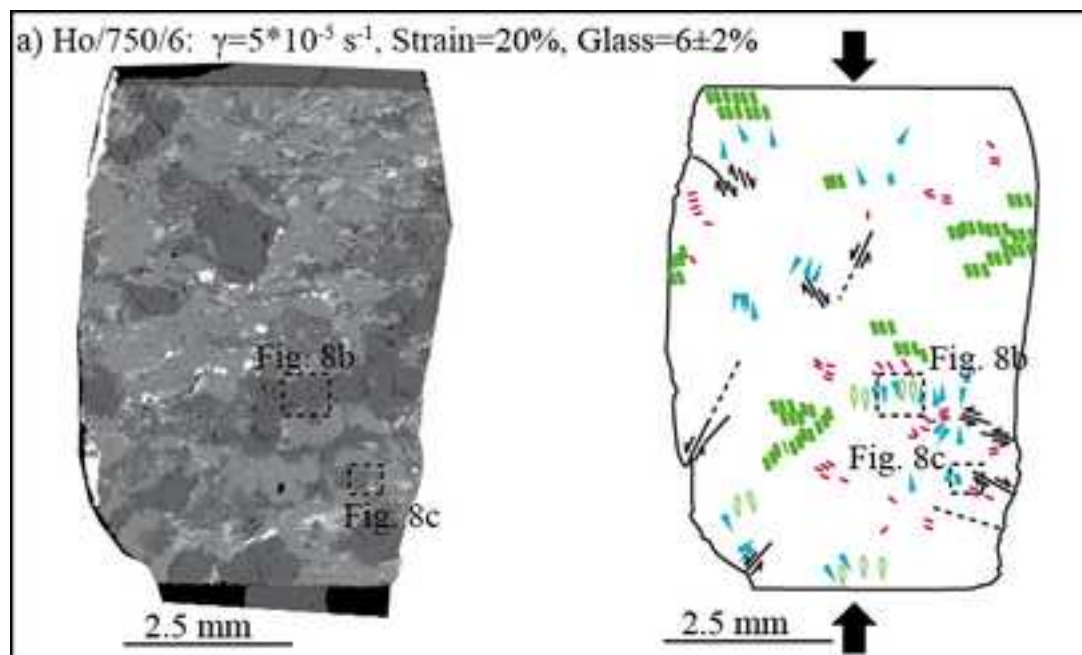


*Figure4

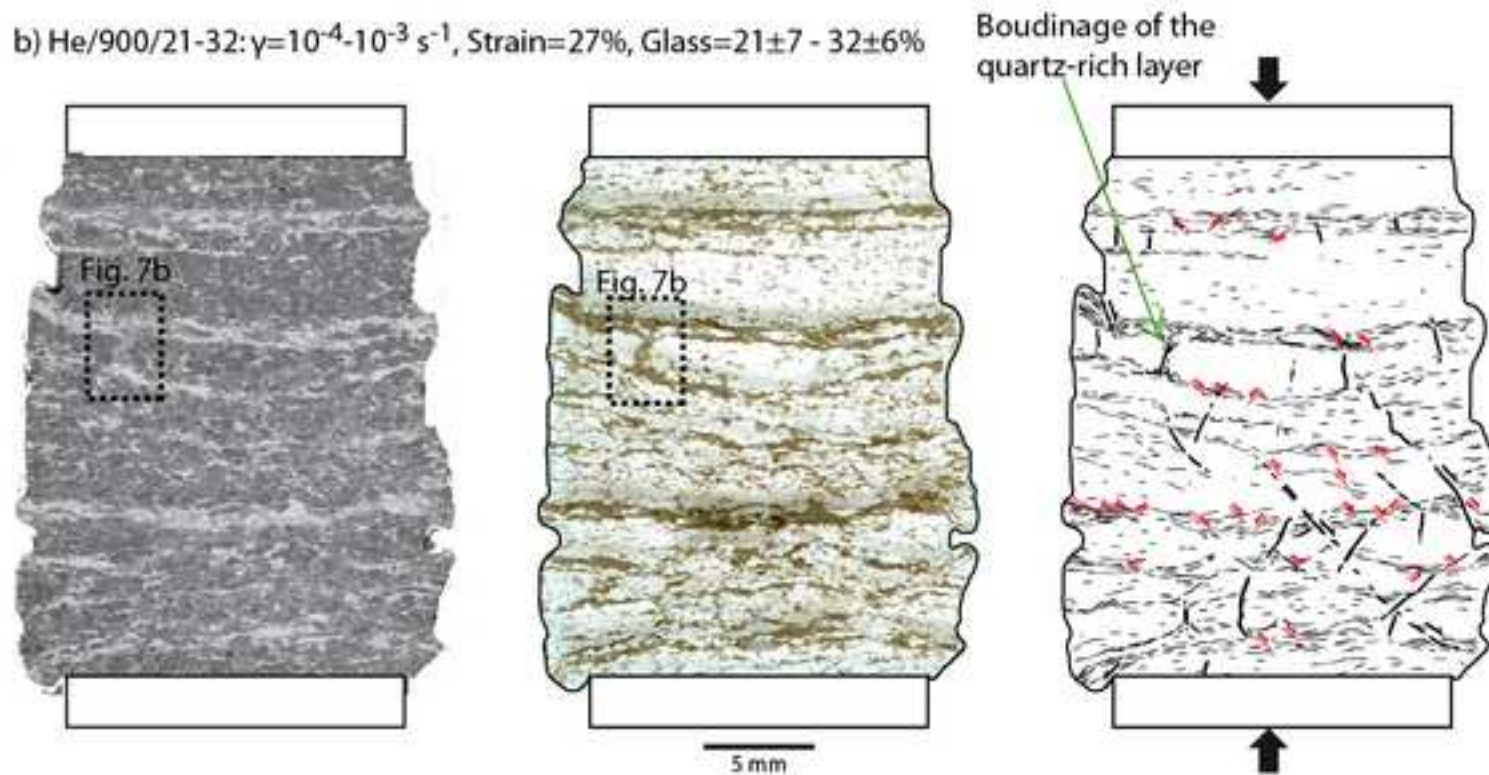
[Click here to download high resolution image](#)



a) He/850/19: $\dot{\gamma}=10^{-4}-10^{-3} \text{ s}^{-1}$, Strain=20%, Glass=19.2±5.7%



b) He/900/21-32: $\dot{\gamma}=10^{-4}-10^{-3} \text{ s}^{-1}$, Strain=27%, Glass=21±7 - 32±6%



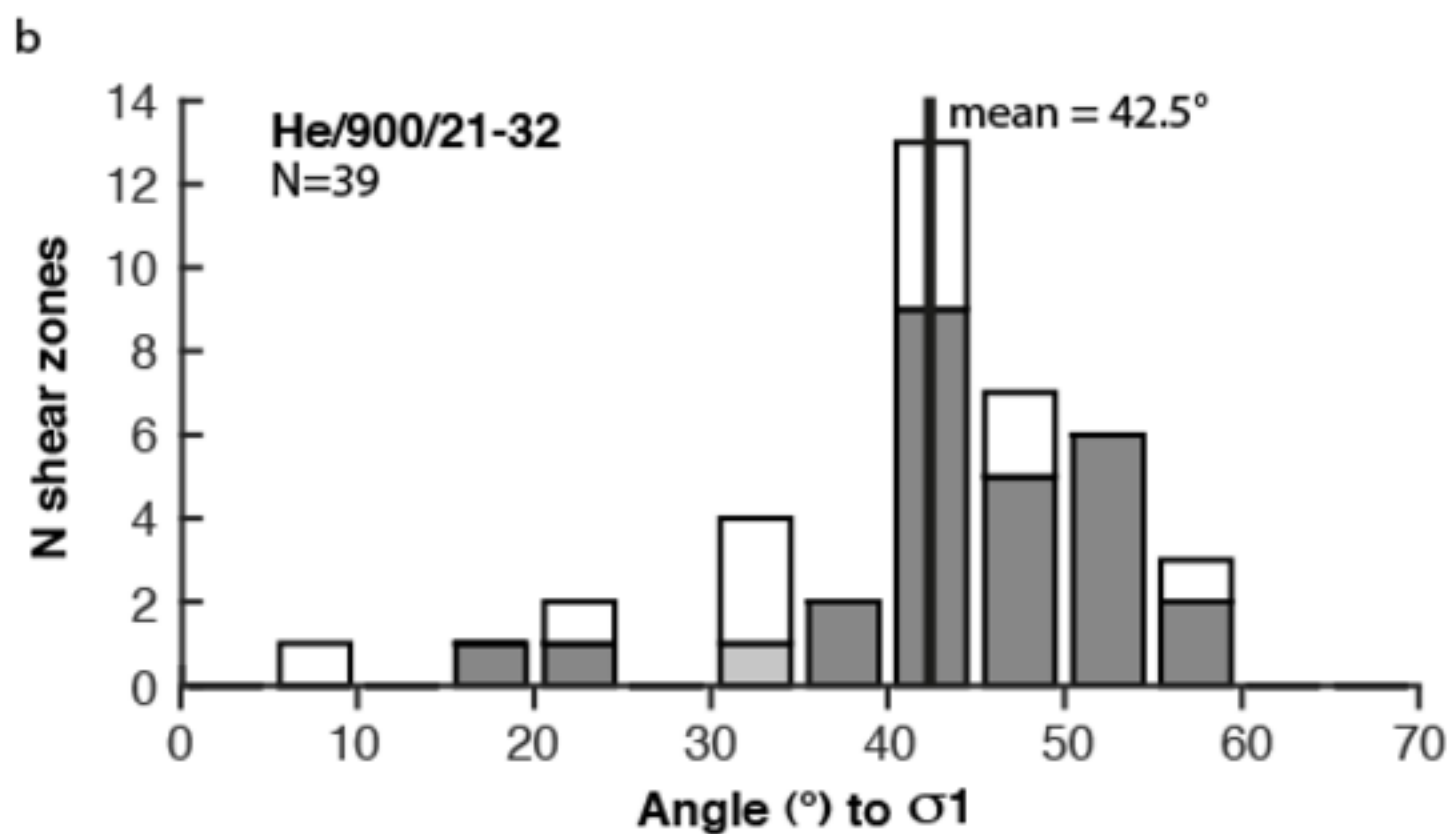
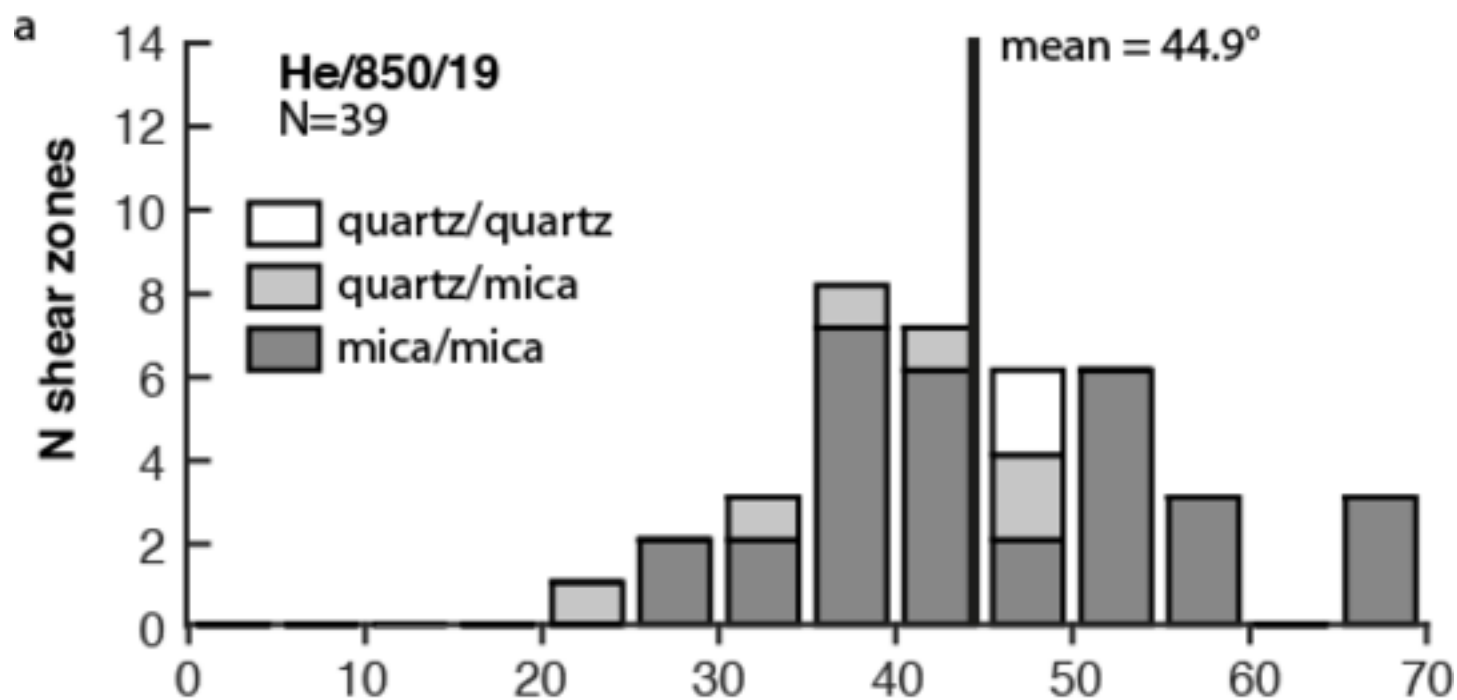


*Figure7
[Click here to download high resolution image](#)

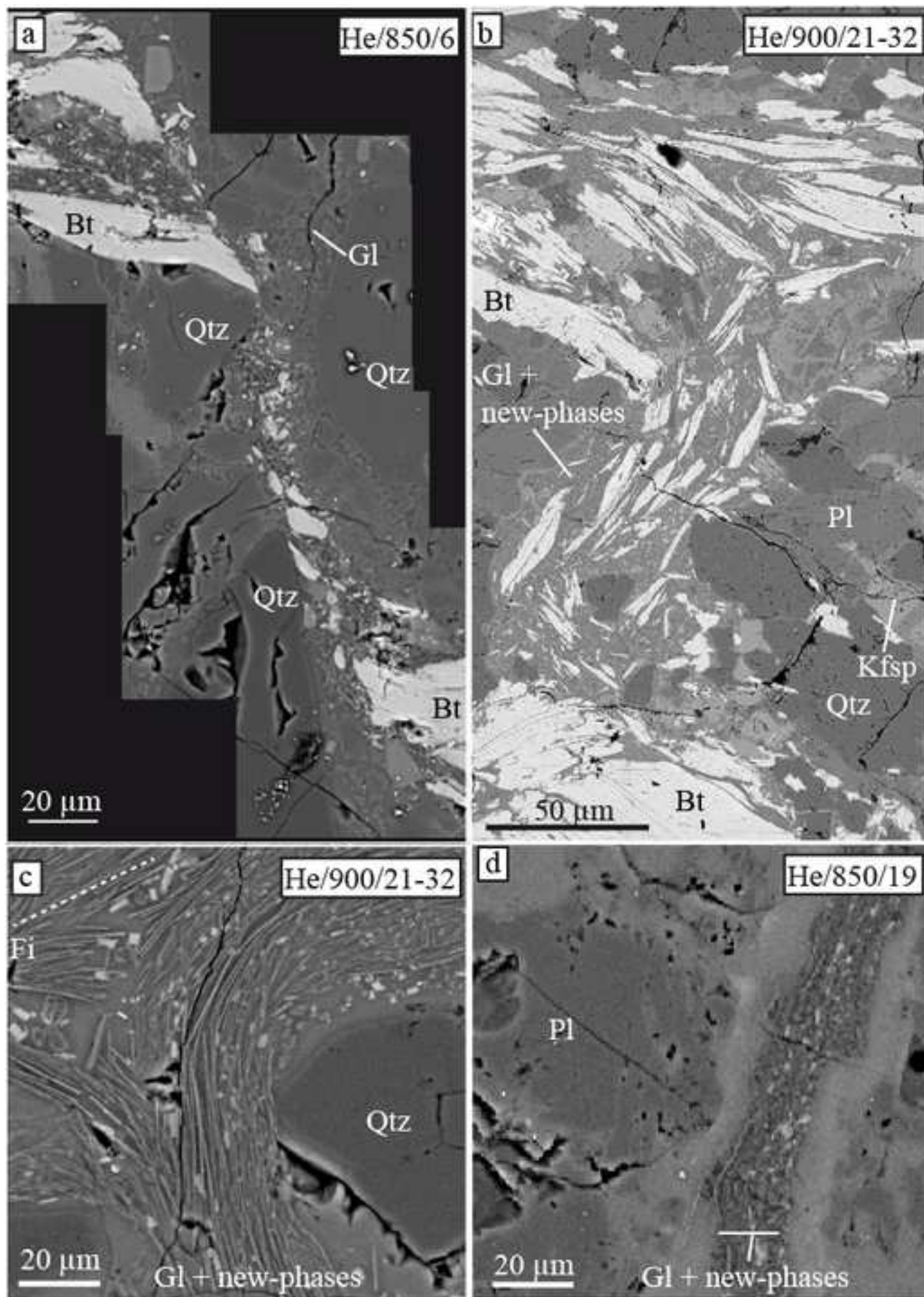


*Figure8
[Click here to download high resolution image](#)

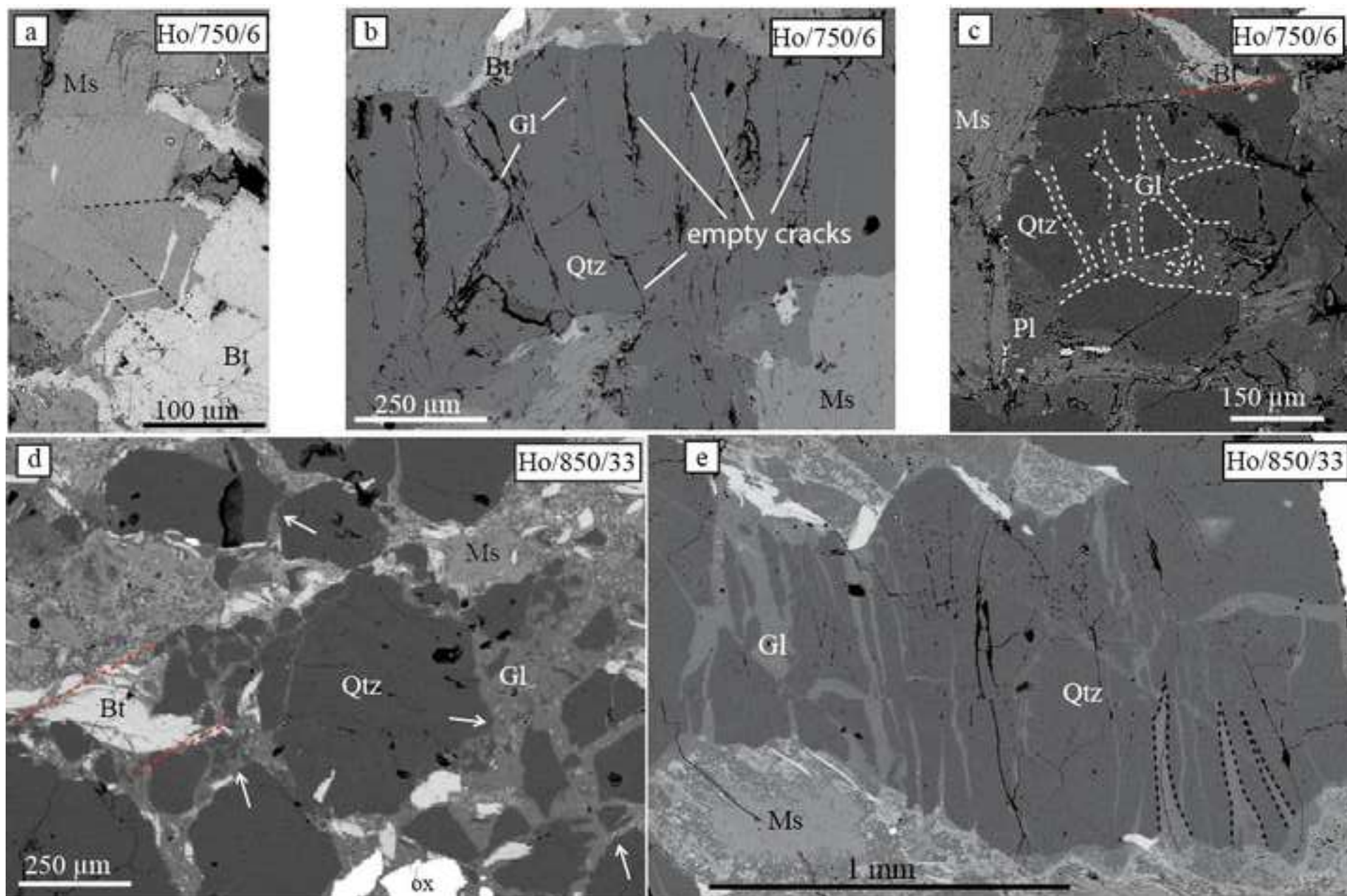


*Figure9
[Click here to download high resolution image](#)

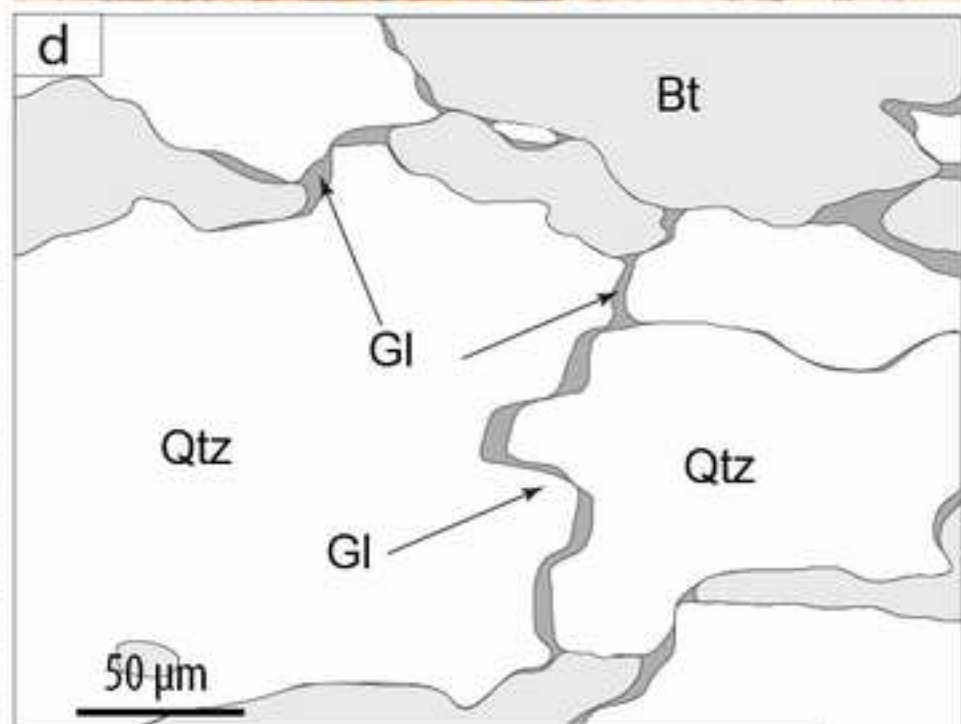
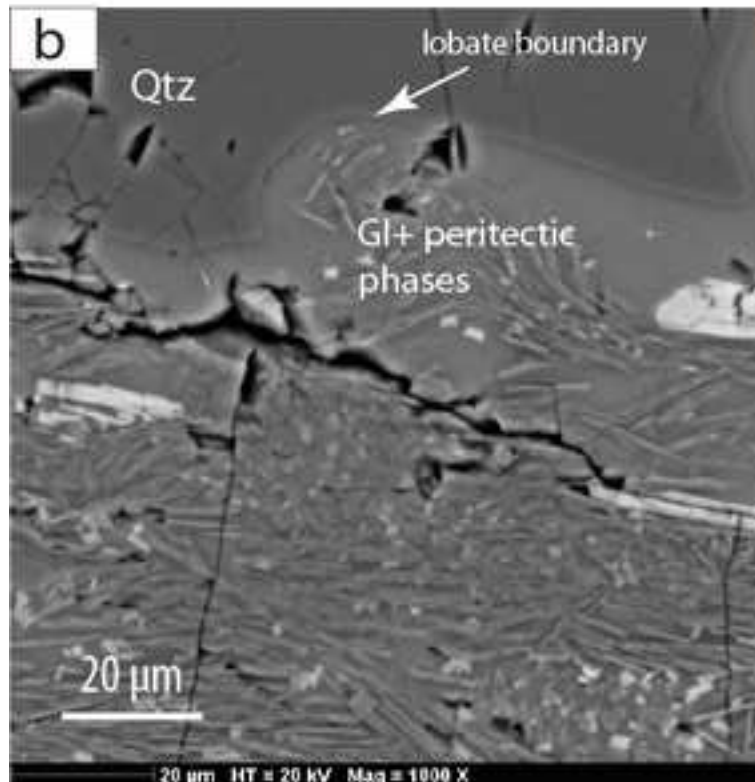
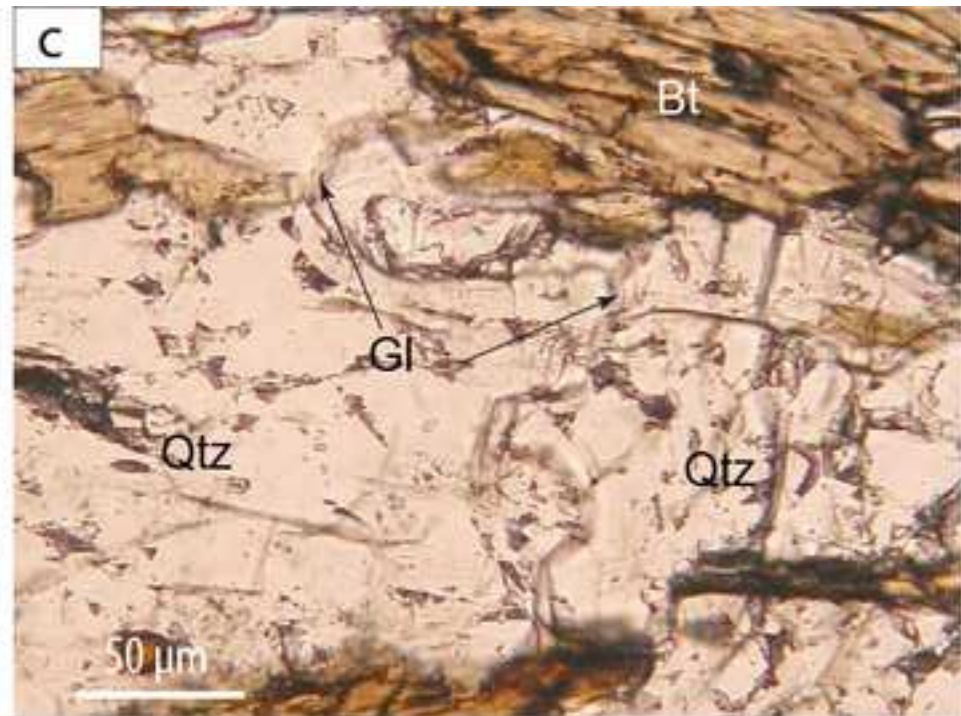
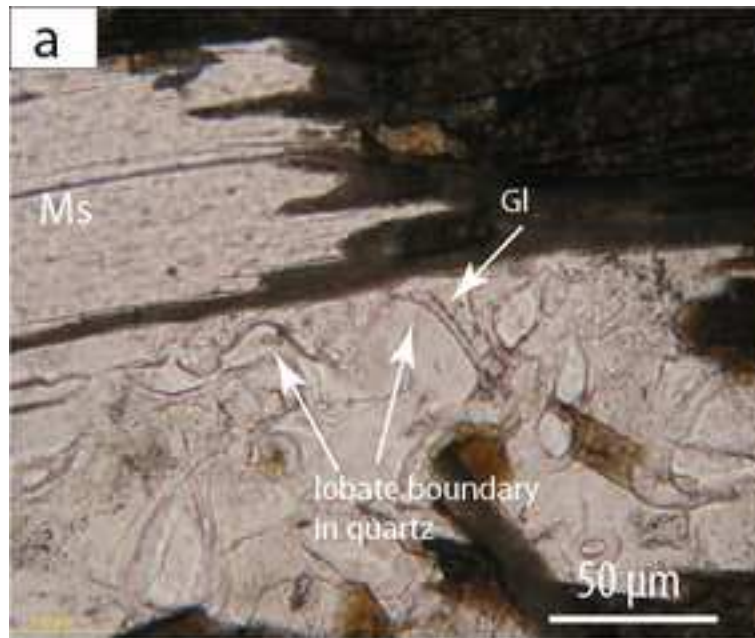
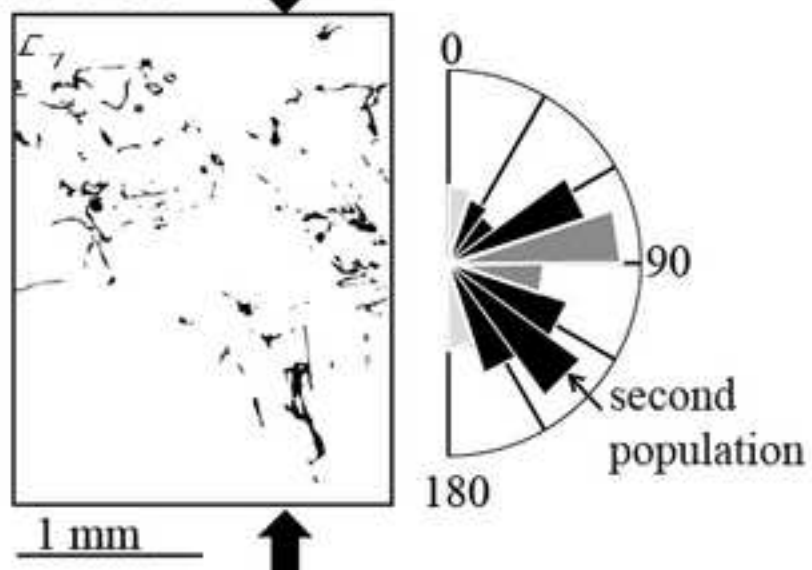


*Figure10

[Click here to download high resolution image](#)

a) Ho/750/6: $\gamma=5 \cdot 10^{-5} \text{ s}^{-1}$; Strain=20% ;
Glass=6 \pm 3%



b) Ho/850/33: $\gamma=10^{-5}-1.25 \cdot 10^{-3} \text{ s}^{-1}$; Strain=11% ;
Glass=33 \pm 4%

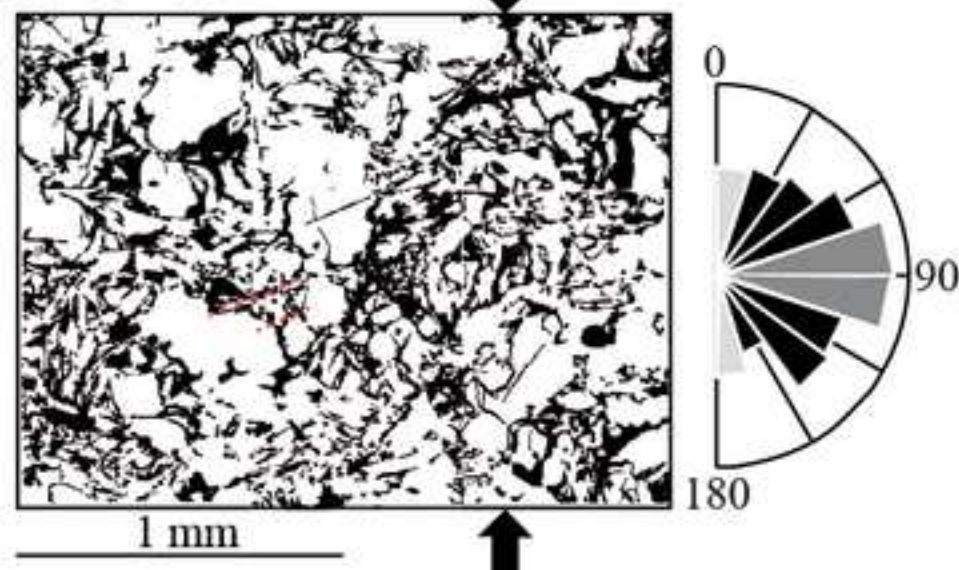


*Figure11

[Click here to download high resolution image](#)

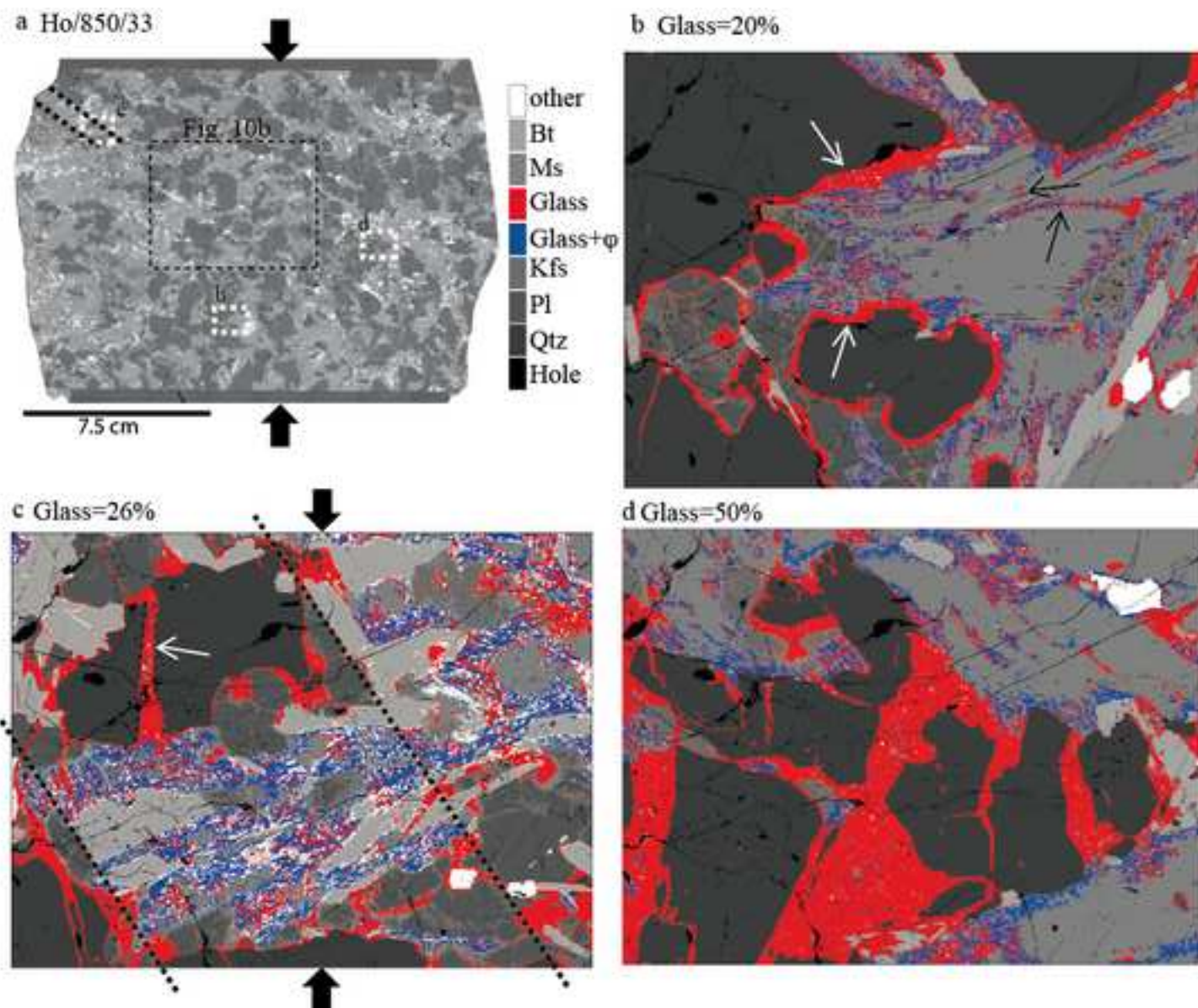
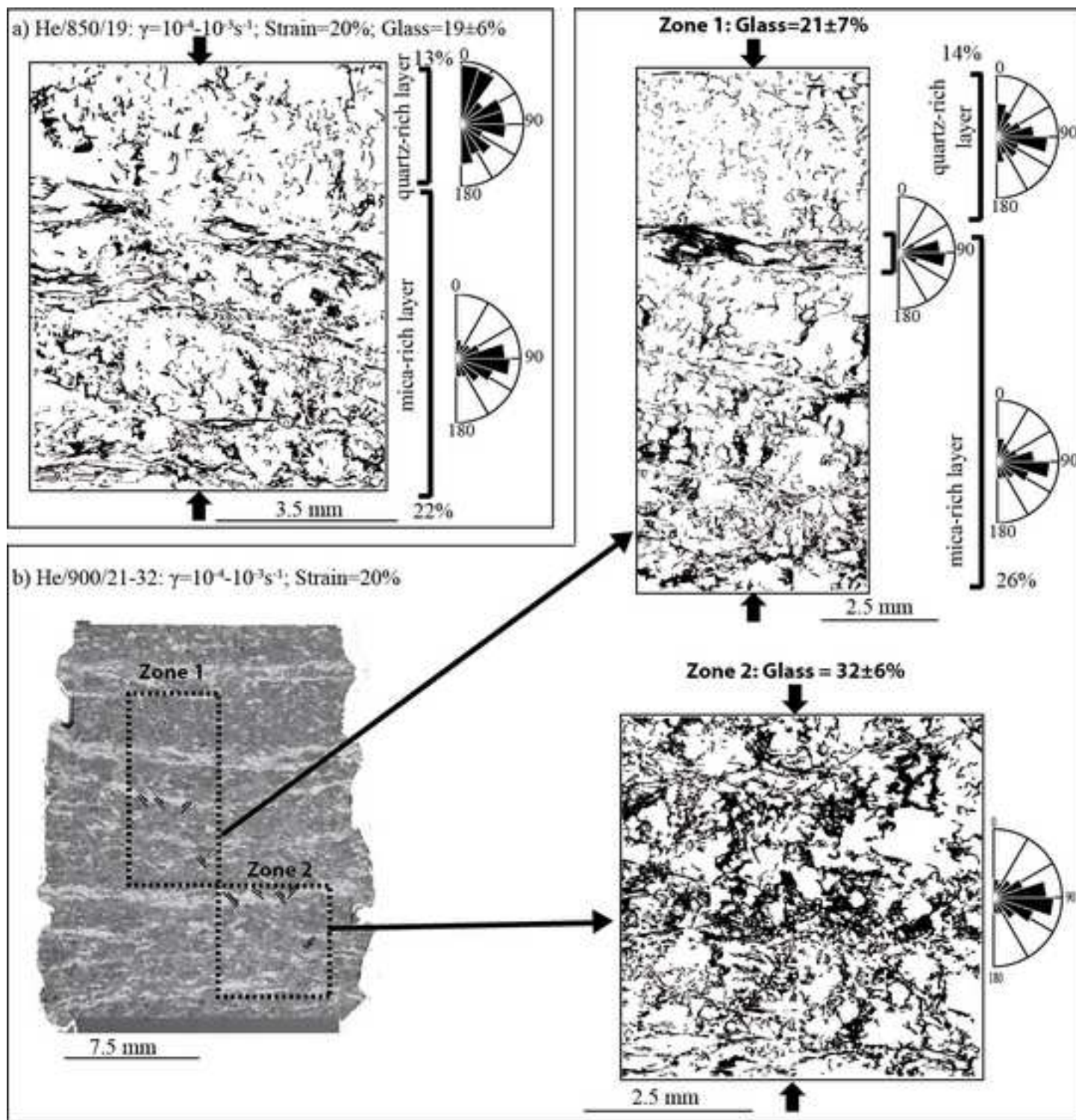
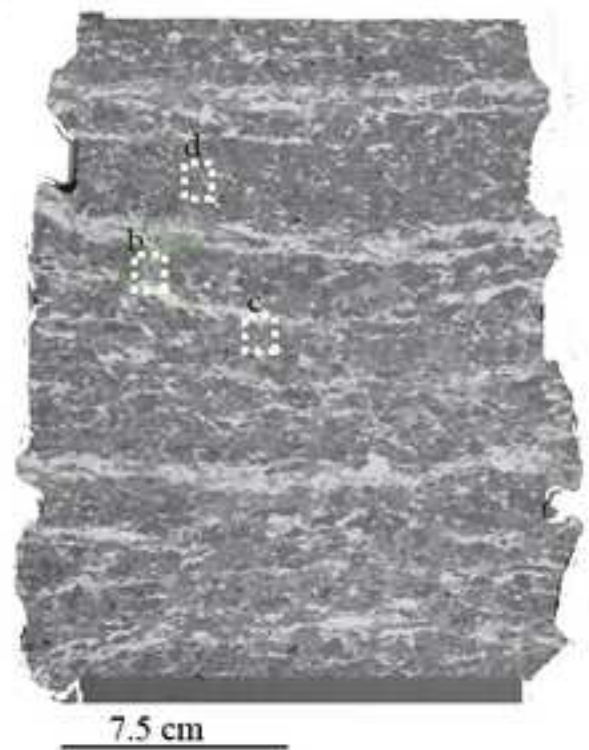


*Figure12

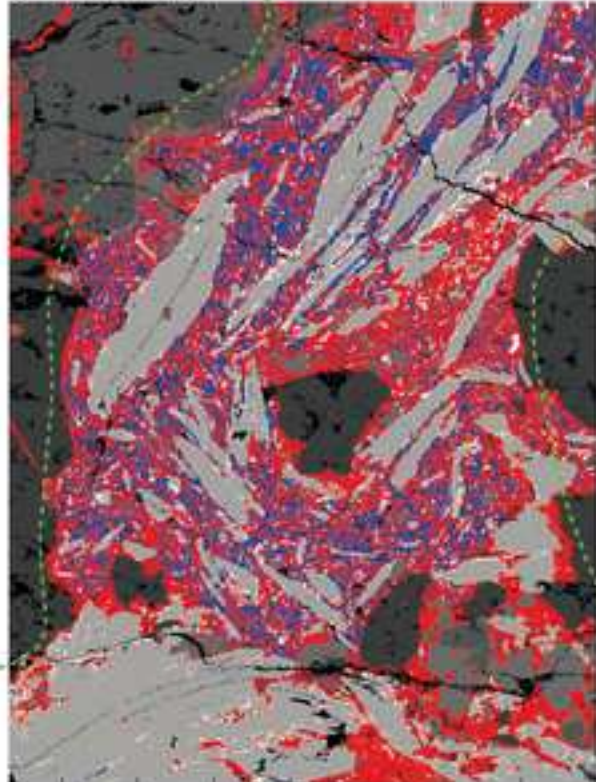
[Click here to download high resolution image](#)



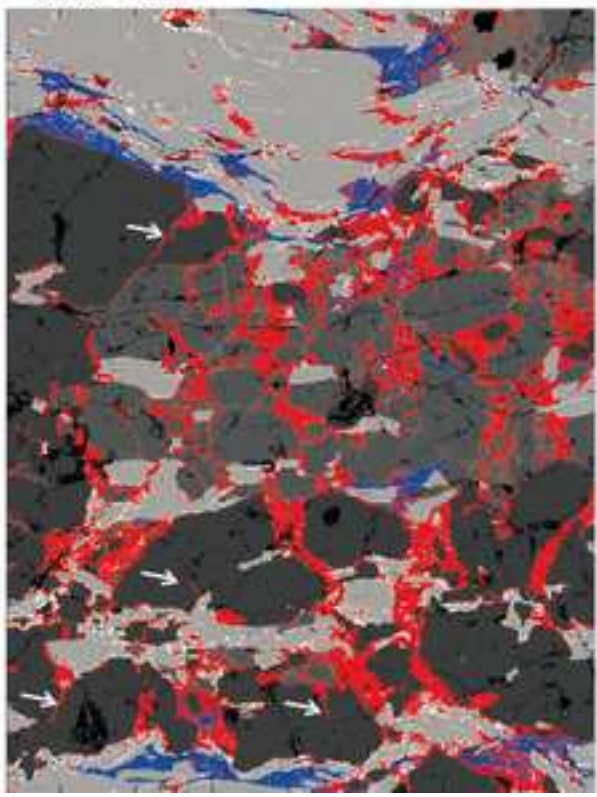
a He/900/21-32



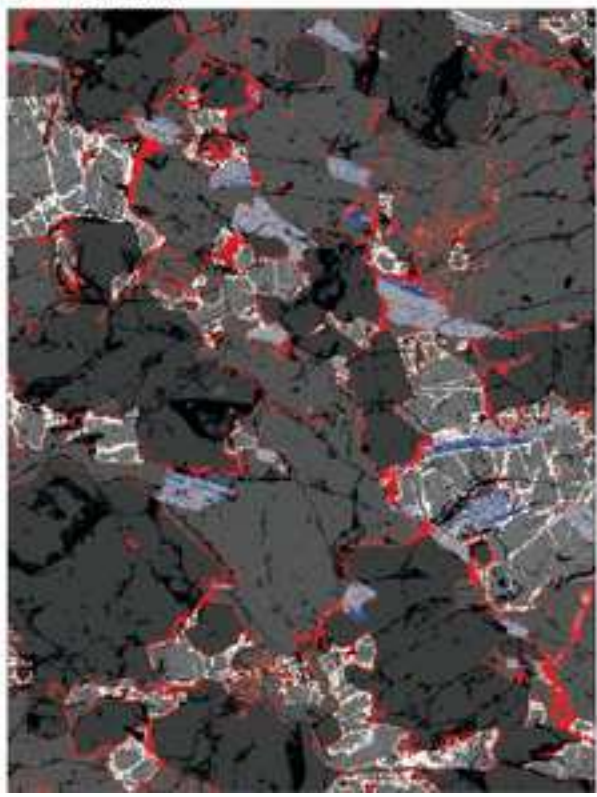
b Melt=41%









c Melt=20%



d Melt=8%



-  other
-  Bt
-  Gl
-  Gl+φ
-  Kfs
-  Pl
-  Qtz
-  hole

*Figure14
[Click here to download high resolution image](#)

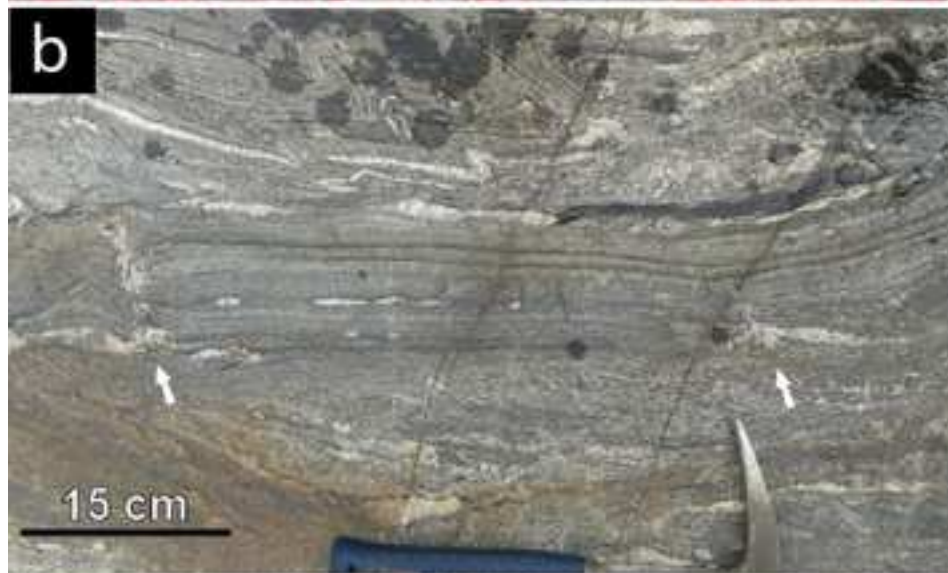


Table1

experiment name	experiment number	starting material	jacket	size diameter (mm) length (mm)		T (°C)	Strain rate (s ⁻¹)	duration (hour)	Strain (%)	melt content (%)
Protolith: NOP1 (Homogeneous)										
Ho/850/33	PP218	NOP1-A	Fe+Pt	15	15.19	850	10 ⁻⁵	0.6	2.1	
							5*10 ⁻⁵	0.3	3	
							2.5*10 ⁻⁴	0.06	3	
							1.25*10 ⁻³	0.02	3	33
Ho/750/6	PP315	NOP1-B	Fe+Cu	5	10.29	750	2*10 ⁻⁵	2.87	20	6
Protolith: PX28 (Heterogeneous)										
-	PP123	-	Fe+Pt	14.91	19.42	850	0.0	1.75	0	unknown
He/900/21-32	PP111	-	Fe+Pt	15	28.8	900	10 ⁻⁴	0.28	10	
							10 ⁻³	0.05	17	21-32
He/850/19	PP113	-	Fe+Pt	15	21.74	850	10 ⁻⁴	0.23	8.4	
							10 ⁻³	0.02	8.8	19